Bulletin of the Earthquake
Research Institute
University of Tokyo
Vol. 62 (1987) pp. 201-245

Synthetic Seismograms in Realistic Media: A Wave-theoretical Approach

Kazuki KOHKETSU

Earthquake Research Institute, University of Tokyo

(Received May 14, 1987)

Abstract

In order to interpret seismograms, we should separate the effects of source and medium, which are strongly coupled. The medium effect is usually estimated by computing synthetic seismograms for a model of the Earth. Of course, a three-dimensionally heterogeneous, arbitrarily anisotropic and attenuative medium is the most realistic model, but it requires a great deal of theoretical and numerical effort. At present one- or two-dimensionally layered, isotropic and attenuative media consisting of homogeneous layers are the most productive models for precise waveform analyses of seismograms. A new approach based on the reflectivity method is presented here to compute complete synthetic seismograms in these models.

Following the standard derivation of the reflectivity method, displacement and stress components are doubly transformed into the frequency-wavenumber domain, and they are treated together in a motion-stress vector. In one-dimensionally layered media which have only flat interfaces, the boundary conditions at the interfaces are simply satisfied by the motion-stress vectors and propagator matrices for individual wavenumbers. Thus synthetic seismograms can be obtained by summing up displacement transforms computed individually. These seismograms include all multiple reflections and surface waves. The effect of Q-values can easily be introduced into them.

In two-dimensionally layered media, on the other hand, scattering by irregular interfaces causes the coupling among different wavenumbers. The boundary conditions are not satisfied for individual wavenumbers, but only for a total wave-field. Then we introduce the Aki-Larner technique to solve the integral equations for these conditions and enlarge the propagator matrices to express the total wave-field.

Numerical examples are presented for several one- and two-dimensionally layered media to confirm the validity of our approach. Some of them compare to the results of other methods, *i.e.* the finite element and difference methods, the asymptotic ray theory, and the Gaussian beam method. Our results agree well with those of the finite element and difference methods even in a later portion where

the latter two methods break down.

In the second half our approach is applied to investigate the effects of the details of crustal structures on synthetic seismograms. Computations for typical models reveal that layers thicker than $\lambda/10$ (λ: wavelength of input signal) cannot be ignored, and interface dents larger than $\lambda/10$ must affect seismograms. Seismograms are also synthesized for the crustal model of the Kanto plain obtained by refraction experiments. They show that the irregular interface strongly affects their waveform and amplitudes.

1. Introduction

Seismologists look at the Earth's interior and earthquake sources through windows called seismograms. Since the effect of medium on seismograms is strongly coupled with the effect of source, the interpretation of seismograms should start with the separation of them. On interpreting amplitudes or waveforms the medium effect is usually estimated from synthetic seismograms computed for a model of the Earth. It is no wonder that a detailed analysis of medium requires synthetic seismograms for a realistic model. Moreover, a source analysis also requires them, because wrong estimations of medium and source effects can produce a result apparently consistent with observation.

Of course a three-dimensionally heterogeneous, arbitrarily anisotropic and attenuative medium is the most realistic model, but it requires a great deal of theoretical and numerical effort. It also has too many parameters to build an initial model, or to obtain significant results from data presently available. One- or two-dimensionally layered media consisting of homogeneous, isotropic and attenuative layers are the most productive models for precise waveform analyses of seismograms.

From the 1960's a number of methods were presented for synthesizing seismograms in layered media. At present it can be said that, except for some computational problems, the theory of seismogram synthesis has been completed for one-dimensionally layered media ($1-D$ media) whose physical properties depend only on depth. Methods for $1-D$ media can be divided into three groups. The first group (*e.g.*, ČERVENÝ and Ravindra 1971; HRON and KANASEWICH 1971) is based on the asymptotic ray theory. Methods of this group are approximate but very fast. The second group, based on wave theory, can generate more accurate seismograms at the cost of longer computation time. The last group is purely numerical and requires much more extensive computation. The general finite difference, finite element, and boundary element methods belong to this group. Recent efforts of theoretical

seismologists were focussed on the second group, *i.e.* wave-theoretical methods. In this group are the Generalized Ray Theory (HELMBERGER 1968; MÜLLER 1969), the WKBJ Theory (CHAPMAN 1978) and the Full Wave Theory (CORMIER and RICHARDS 1977), which can compute seismograms for specified phases. On the other hand the reflectivity method can generate complete seismograms including all body and surface waves. In its original version (FUCHS 1968; FUCHS and MÜLLER 1971) a few approximations still remained, but they will be removed in this paper following the formulation of KIND (1978).

In the reflectivity method a doubly transformed wave-field is computed using propagator matrices, and seismograms are obtained by numerical inverse transforms. The transformed wave-field is expressed by a linear combination of reflectivities (generalized reflection coefficients) in the original reflectivity method and its revisions (*e.g.*, FABER and MÜLLER 1980; KOHKETSU 1981), but reflectivities do not explicitly appear in the complete wave-field of the extended version described hereafter. However, KENNETT and KERRY (1979) have shown that the latter wave-field implicitly includes reflectivities for all parts of a layered medium. Thus, following AKI and RICHARDS (1980), we suggest that all methods where transformed wave-fields are evaluated with matrices and inverted numerically will be referred to as *Reflectivity Methods*.

The reflectivity method has many variations. Some authors modified propagator matrices to avoid numerical instabilities at high frequencies (*e.g.*, KENNETT 1980; HA 1984), and others deformed the integration contour of inverse transform to improve convergence (*e.g.*, WANG and HERRMANN 1980; SATO and HIRATA, 1980). BOUCHON (1979) and CORMIER (1980) replace the Hankel transform with the double Fourier and the spherical harmonic transforms to apply the method to rectangular faults and the spherical Earth. The 'Discrete Wavenumber Method' of BOUCHON (1981) and the 'Wavenumber Integration Method' of APSEL and LUCO (1983) are essentially identical to the reflectivity method. The modal summation method (*e.g.*, HARKRIDER 1964; HARVEY 1981) is a distant relative with residue approximation for numerical inverse transforms. The Alekseev-Mikhailenko method (ALEKSEEV and MIKHAILENKO 1980), the collocation method (SPUDICH and ASCHER 1983), and the discrete wavenumber/finite element method (OLSON *et al.* 1984) can be called half-breeds of the reflectivity method and purely numerical approaches.

Here it should be noted that the reflectivity method has been able to be applied to $1-D$ media. At present, however, seismologists and geophysicists are strongly interested in the Earth's laterally hetero-

geneous structure. Synthetic seismograms used in analyses of the lateral heterogeneity are usually computed by the asymptotic ray/beam method (*e.g.*, ČERVENÝ *et al.* 1977; ČERVENÝ 1983) or purely numerical methods (*e.g.*, BOORE 1970; SMITH 1975). The former contains many serious approximations, and the latter requires extensive computations and large core storage. Wave-theoretical approaches, especially the reflectivity method, may be superior to the above method's cost-accuracy trade-off. In the second chapter of this paper the reflectivity method will be extended to the complete seismogram synthesis in $1-D$ media and two-dimensionally layered media with laterally varying interfaces ($2-D$ media).

In the third chapter our method will be applied to investigate the effects of the details of crustal structures on synthetic seismograms. Thin layers in the shallow part of the crust and fluctuations on interfaces are usually ignored, but they must influence seismograms in some situations. By numerical simulations it will be shown how thick layers and how large fluctuations on interfaces can affect synthetic seismograms.

Finally, synthetic seismograms will be computed for the actual structure beneath the Kanto plain. The two-dimensional structure of attenuative sediments will be derived and its effects will be estimated by comparing synthetic seismograms for a variety of crustal models.

2. Method

In this chapter we will derive the double integral transform of the surface displacement due to an incident plane wave, a line source or a point source in $1-D$ and $2-D$ media. To a possible extent we will follow KOHKETSU'S (1987) formulations for SH waves. We will then rewrite this transform in a matrix form so that it can be inverted numerically by a digital computer. Examples of synthetic seismograms will also be presented and some of them will be compared to the results of other methods in order to confirm the validity of our method.

2.1 Boundary condition

The considered medium consists of $M-1$ layers overlying a halfspace. The halfspace will sometimes be called the M-th layer. A Cartesian coordinate system (x, y, z) is used with z-axis taken position downward (Fig. 2.1). Each layer is isotropic and homogeneous with P-wave velocity α_k, S-wave velocity β_k, and density $\rho_k (k=1, \cdots, M)$. If a layer is attenuative, we should take the following complex velocity models:

$$\alpha_k=\alpha_k^0\left[1+\frac{1}{\pi Q_{\alpha k}}\ln\left(\frac{\omega}{\omega_0}\right)-\frac{j}{2Q_{\alpha k}}\right],$$

$$\beta_k=\beta_k^0\left[1+\frac{1}{\pi Q_{\beta k}}\ln\left(\frac{\omega}{\omega_0}\right)-\frac{j}{2Q_{\beta k}}\right] \qquad (1)$$

where $j=\sqrt{-1}$, and $Q_{\alpha k}$, $Q_{\beta k}$ are the Q values of P and S waves for the k-th layer, respectively. α_k^0, β_k^0 are the P, S wave velocities of the k-th layer at $\omega=\omega_0$. The free surface and interfaces separating the layers have laterally irregular shapes expressed by the depth function:

$$z_k(x)=z_k^0+h_k(x) \quad (k=0, \cdots, M-1), \qquad (2)$$

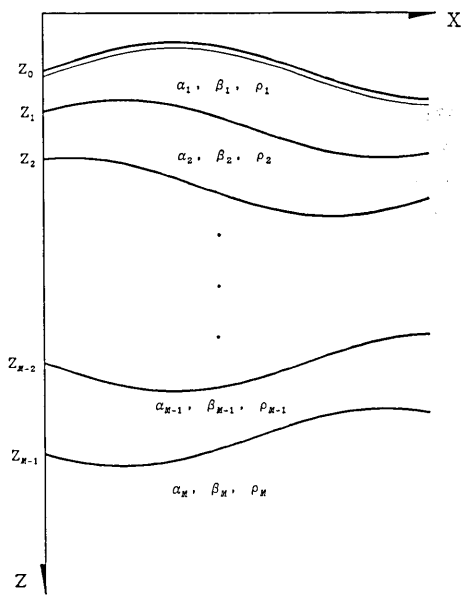

Fig. 2.1. A layered medium consisting of $M-1$ layers and a halfspace. The k-th layer with material parameters α_k, β_k and ρ_k is bounded by the $(k-1)$-th and k-th interfaces at the depths of z_{k-1} and z_k. The solid line associated with a thin line is the free surface.

which fluctuates around the average depth z_k^0 with the function $h_k(x)$. The average thickness of the k-th layer is $d_k=z_k^0-z_{k-1}^0$.

We consider plane waves whose initial direction of propagation is confined in the $x-z$ plane. Since their motion will be independent of y at any time in our $2-D$ media, the wave-field as well as the medium properties are functions only of x and z. The elastic displacement $[u, v, w]$ can be expressed by

$$\left[\frac{\partial\varphi}{\partial x}-\frac{\partial\phi}{\partial z}, \quad v(x, z, t), \quad \frac{\partial\varphi}{\partial z}+\frac{\partial\phi}{\partial x}\right] \qquad (3)$$

with the P-wave potential $\varphi(x, z, t)$ and the SV-wave one $\phi(x, z, t)$. $v(x, z, t)$ represents a displacement of SH wave. Since the wave-field is independent of y, stress components are reduced as

$$\tau_{xx}=(\lambda+2\mu)\frac{\partial u}{\partial x}+\lambda\frac{\partial w}{\partial z}, \quad \tau_{yy}=\lambda\left(\frac{\partial u}{\partial x}+\frac{\partial w}{\partial z}\right)$$

$$\tau_{zz}=\lambda\frac{\partial u}{\partial x}+(\lambda+2\mu)\frac{\partial w}{\partial z}, \quad \tau_{xz}=\mu\left(\frac{\partial u}{\partial z}+\frac{\partial w}{\partial x}\right)$$

$$\tau_{yz}=\mu\frac{\partial v}{\partial z}\,, \qquad \tau_{xy}=\mu\frac{\partial v}{\partial x}\,, \tag{4}$$

where λ and μ are Lamé's constants. The four upper components are due to the $P-SV$ wave, and the two lowers due to the SH wave. Following the standard derivation of the reflectivity method, we doubly transform the potentials, displacements and stresses into the frequency-wavenumber $(\omega-k)$ domain as

$$\begin{aligned}
\varphi(x,z,t) &= \frac{1}{2\pi}\int_{-\infty}^{+\infty}\bar{\varphi}(x,z,\omega)e^{j\omega t}d\omega\\
\phi(x,z,t) &= \frac{1}{2\pi}\int_{-\infty}^{+\infty}\bar{\phi}(x,z,\omega)e^{j\omega t}d\omega\\
u(x,z,t) &= \frac{1}{2\pi}\int_{-\infty}^{+\infty}\bar{u}(x,z,\omega)e^{j\omega t}d\omega\\
w(x,z,t) &= \frac{1}{2\pi}\int_{-\infty}^{+\infty}\bar{w}(x,z,\omega)e^{j\omega t}d\omega\\
\tau_{zz}(x,z,t) &= \frac{1}{2\pi}\int_{-\infty}^{+\infty}\bar{s}(x,z,\omega)e^{j\omega t}d\omega\\
\tau_{zx}(x,z,t) &= \frac{1}{2\pi}\int_{-\infty}^{+\infty}\bar{t}(x,z,\omega)e^{j\omega t}d\omega\\
v(x,z,t) &= \frac{1}{2\pi}\int_{-\infty}^{+\infty}\bar{v}(x,z,\omega)e^{j\omega t}d\omega\\
\tau_{zy}(x,z,t) &= \frac{1}{2\pi}\int_{-\infty}^{+\infty}\bar{p}(x,z,\omega)e^{j\omega t}d\omega\,,
\end{aligned} \tag{5}$$

and

$$\begin{aligned}
\bar{\varphi}(x,z,\omega) &= \frac{1}{2\pi}\int_{-\infty}^{+\infty}\tilde{\varphi}(k,z,\omega)e^{jkx}dk\\
\bar{\phi}(x,z,\omega) &= \frac{1}{2\pi}\int_{-\infty}^{+\infty}\tilde{\phi}(k,z,\omega)e^{jkx}dk\\
\bar{u}(x,z,\omega) &= \frac{1}{2\pi}\int_{-\infty}^{+\infty}\tilde{u}(k,z,\omega)e^{jkx}dk\\
\bar{w}(x,z,\omega) &= \frac{1}{2\pi}\int_{-\infty}^{+\infty}\tilde{w}(k,z,\omega)e^{jkx}dk\\
\bar{s}(x,z,\omega) &= \frac{1}{2\pi}\int_{-\infty}^{+\infty}\tilde{s}(k,z,\omega)e^{jkx}dk\\
\bar{t}(x,z,\omega) &= \frac{1}{2\pi}\int_{-\infty}^{+\infty}\tilde{t}(k,z,\omega)e^{jkx}dk
\end{aligned}$$

$$\bar{v}(x, z, \omega) = \frac{1}{2\pi}\int_{-\infty}^{+\infty} \tilde{v}(k, z, \omega) e^{jkx} dk$$

$$\bar{p}(x, z, \omega) = \frac{1}{2\pi}\int_{-\infty}^{+\infty} \tilde{p}(k, z, \omega) e^{jkx} dk \ . \qquad (6)$$

As in (4), the six upper transforms in (5) and (6) belong to the $P-SV$ wave, and the two lower to the SH wave. Since φ, ϕ and v satisfy the wave equations

$$\alpha^2 \nabla^2 \varphi = \frac{\partial^2 \varphi}{\partial t^2}$$

$$\beta^2 \nabla^2 \phi = \frac{\partial^2 \phi}{\partial t^2}$$

$$\beta^2 \nabla^2 v = \frac{\partial^2 v}{\partial t^2} \ ,$$

$\tilde{\varphi}$, $\tilde{\phi}$ and $\tilde{v}$ should have the form

$$\begin{aligned} \tilde{\varphi} &= A_- e^{+j\nu_\alpha z} + A_+ e^{-j\nu_\alpha z} \\ \tilde{\phi} &= B_- e^{+j\nu_\beta z} + B_+ e^{-j\nu_\beta z} \\ \tilde{v} &= C_- e^{+j\nu_\beta z} + C_+ e^{-j\nu_\beta z} \ , \end{aligned} \qquad (7)$$

where

$$\nu_v = \begin{cases} \sqrt{k_v^2 - k^2} & k_v > k \\ -j\sqrt{k^2 - k_v^2} & k_v < k \ , \end{cases} \qquad k_v = \frac{\omega}{v} \ .$$

v represents the P wave velocity (α) or the S wave velocity (β).

When an upper layer with α_1, β_1 and ρ_1 is separated from the lower with α_2, β_2 and ρ_2 by the interface at $z(x)=z^0+h(x)$ (Fig. 2.2),

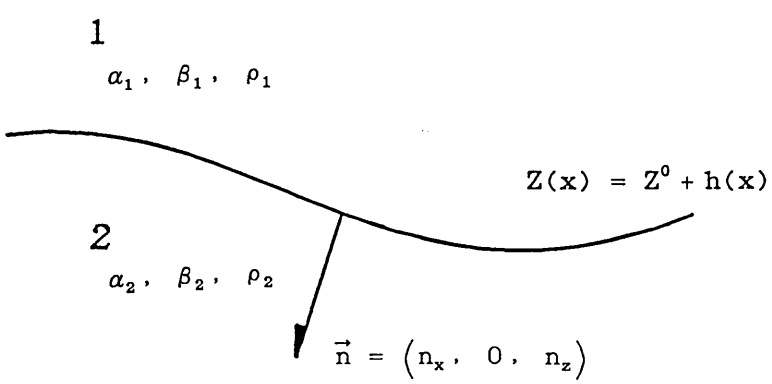

Fig. 2.2. An irregular interface between two layers. $\vec{n}$ is the unit normal to the interface.

the condition of continuity must be imposed along the interface. The condition for continuity of displacement

$$\begin{aligned}
&\int_{-\infty}^{+\infty} \tilde{u}_1(k,\ z(x),\ \omega)e^{jkx}dk = \int_{-\infty}^{+\infty} \tilde{u}_2(k,\ z(x),\ \omega)e^{jkx}dk \\
&\int_{-\infty}^{+\infty} \tilde{w}_1(k,\ z(x),\ \omega)e^{jkx}dk = \int_{-\infty}^{+\infty} \tilde{w}_2(k,\ z(x),\ \omega)e^{jkx}dk \\
&\int_{-\infty}^{+\infty} \tilde{v}_1(k,\ z(x),\ \omega)e^{jkx}dk = \int_{-\infty}^{+\infty} \tilde{v}_2(k,\ z(x),\ \omega)e^{jkx}dk
\end{aligned} \tag{8}$$

has to be satisfied for every x. If $z \equiv z^0$, *i.e.* the interface is horizontal ($1-D$ media), kernels are independent of x, and These integral equations will simply be solved as

$$\begin{aligned}
&\tilde{u}_1(k,\ z^0,\ \omega) = \tilde{u}_2(k,\ z^0,\ \omega) \\
&\tilde{w}_1(k,\ z^0,\ \omega) = \tilde{w}_2(k,\ z^0,\ \omega) \\
&\tilde{v}_1(k,\ z^0,\ \omega) = \tilde{v}_2(k,\ z^0,\ \omega)\ .
\end{aligned} \tag{9}$$

For an irregular interface, however, we have no trivial solutions like (9). In other words, scattering by irregular interfaces causes the coupling among different wavenumbers. AKI and LARNER (1970) found a practical way to solve (8) for irregular interfaces, but their formulation is restricted to one-interface problems. In the present paper we will extend it to the reflectivity method for multilayered media. After insertion of (7) and (2) into (6), we now approximate the infinite integrals of $\bar{u}$, $\bar{w}$ and $\bar{v}$ in (6) by the finite sums

$$\begin{aligned}
&\frac{\Delta k}{2\pi} \sum_{n=-N}^{N-1} [{}^x_P H^n_{-P} X^n_- + {}^x_P H^n_{+P} X^n_+ + {}^x_V H^n_{-V} X^n_- + {}^x_V H^n_{+V} X^n_+] e^{jn\Delta kx} \\
&\frac{\Delta k}{2\pi} \sum_{n=-N}^{N-1} [{}^z_P H^n_{-P} X^n_- + {}^z_P H^n_{+P} X^n_+ + {}^z_V H^n_{-V} X^n_- + {}^z_V H^n_{+V} X^n_+] e^{jn\Delta kx} \\
&\frac{\Delta k}{2\pi} \sum_{n=-N}^{N-1} [{}_H H^n_{-H} X^n_- + {}_H H^n_{+H} X^n_+] e^{jn\Delta kx}
\end{aligned} \tag{10}$$

with

$$\begin{aligned}
&{}^x_P H^n_\pm = jn\Delta k e^{\mp j\nu_{\alpha n} h(x)}\ , \quad {}^x_V H^n_\pm = \pm j\nu_{\beta n} e^{\mp j\nu_{\beta n} h(x)} \\
&{}^z_P H^n_\pm = \mp j\nu_{\alpha n} e^{\mp j\nu_{\alpha n} h(x)}\ , \quad {}^z_V H^n_\pm = jn\Delta k e^{\mp j\nu_{\beta n} h(x)} \\
&{}_P X^n_\pm = A^n_\pm e^{\mp j\nu_{\beta n} z^0}\ , \quad {}_V X^n_\pm = B^n_\pm e^{\mp j\nu_{\beta n} z^0} \\
&{}_H H^n_\pm = e^{\mp j\nu_{\beta n} h(x)}\ , \\
&{}_H X^n_\pm = C^n_\pm e^{\mp j\nu_{\beta n} z^0}
\end{aligned}$$

where $\nu_{vn} = \nu_v|_{k=n\Delta k} (v = \alpha, \beta)$. We next insert (10) into the boundary condition (8) and take the Fourier transform of both sides with respect to x, then we have

$$\sum_{n=-N}^{N-1}\left[{}_{P}^{x}H_{1-P}^{mn}X_{1-}^{n}+{}_{P}^{x}H_{1+P}^{mn}X_{1+}^{n}+{}_{V}^{x}H_{1-V}^{mn}X_{1-}^{n}+{}_{V}^{x}H_{1+V}^{mn}X_{1+}^{n}\right]$$
$$=\sum_{n=-N}^{N-1}\left[{}_{P}^{x}H_{2-P}^{mn}X_{2-}^{n}+{}_{P}^{x}H_{2+P}^{mn}X_{2+}^{n}+{}_{V}^{x}H_{2-V}^{mn}X_{2-}^{n}+{}_{V}^{x}H_{2+V}^{mn}X_{2+}^{n}\right]$$
$$\sum_{n=-N}^{N-1}\left[{}_{P}^{z}H_{1-P}^{mn}X_{1-}^{n}+{}_{P}^{z}H_{1+P}^{mn}X_{1+}^{n}+{}_{V}^{z}H_{1-V}^{mn}X_{1-}^{n}+{}_{V}^{z}H_{1+V}^{mn}X_{1+}^{n}\right]$$
$$=\sum_{n=-N}^{N-1}\left[{}_{P}^{z}H_{2-P}^{mn}X_{2-}^{n}+{}_{P}^{z}H_{2+P}^{mn}X_{2+}^{n}+{}_{V}^{z}H_{2-V}^{mn}X_{2-}^{n}+{}_{V}^{z}H_{2+V}^{mn}X_{2+}^{n}\right]$$
$$\sum_{n=-N}^{N-1}\left[{}_{H}H_{1-H}^{mn}X_{1-}^{n}+{}_{H}H_{1+H}^{mn}X_{1+}^{n}\right]=\sum_{n=-N}^{N-1}\left[{}_{H}H_{2-H}^{mn}X_{2-}^{n}+{}_{H}H_{2+H}^{mn}X_{2+}^{n}\right],$$
$$m=-N,\ -N+1,\ \cdots,\ N-1$$
$$H^{mn}=\frac{\Delta k}{2\pi}\int_{-\infty}^{+\infty}H^{n}e^{j(n-m)\Delta kx}dx\ . \tag{11}$$

(11) are a system of $4N$ simultaneous linear equations for the $P-SV$ wave, and a system of $2N$ equations for the SH wave. They can be rewritten in a matrix form as

$$\begin{bmatrix} {}_{P}^{x}\boldsymbol{H}_{1-} & {}_{V}^{x}\boldsymbol{H}_{1-} & {}_{P}^{x}\boldsymbol{H}_{1+} & {}_{V}^{x}\boldsymbol{H}_{1+} \\ {}_{P}^{z}\boldsymbol{H}_{1-} & {}_{V}^{z}\boldsymbol{H}_{1-} & {}_{P}^{z}\boldsymbol{H}_{1+} & {}_{V}^{z}\boldsymbol{H}_{1+} \end{bmatrix}\begin{bmatrix} {}_{P}\boldsymbol{\Phi}_{1-} \\ {}_{V}\boldsymbol{\Phi}_{1-} \\ {}_{P}\boldsymbol{\Phi}_{1+} \\ {}_{V}\boldsymbol{\Phi}_{1+} \end{bmatrix}=\begin{bmatrix} {}_{P}^{x}\boldsymbol{H}_{2-} & {}_{V}^{x}\boldsymbol{H}_{2-} & {}_{P}^{x}\boldsymbol{H}_{2+} & {}_{V}^{x}\boldsymbol{H}_{2+} \\ {}_{P}^{z}\boldsymbol{H}_{2-} & {}_{V}^{z}\boldsymbol{H}_{2-} & {}_{P}^{z}\boldsymbol{H}_{2+} & {}_{V}^{z}\boldsymbol{H}_{2+} \end{bmatrix}\begin{bmatrix} {}_{P}\boldsymbol{\Phi}_{2-} \\ {}_{V}\boldsymbol{\Phi}_{2-} \\ {}_{P}\boldsymbol{\Phi}_{2+} \\ {}_{V}\boldsymbol{\Phi}_{2+} \end{bmatrix}$$
$$\begin{bmatrix} {}_{H}\boldsymbol{H}_{1-} & {}_{H}\boldsymbol{H}_{1+} \end{bmatrix}\begin{bmatrix} {}_{H}\boldsymbol{\Phi}_{1-} \\ {}_{H}\boldsymbol{\Phi}_{1+} \end{bmatrix}=\begin{bmatrix} {}_{H}\boldsymbol{H}_{2-} & {}_{H}\boldsymbol{H}_{2+} \end{bmatrix}\begin{bmatrix} {}_{H}\boldsymbol{\Phi}_{2-} \\ {}_{H}\boldsymbol{\Phi}_{2+} \end{bmatrix} \tag{12}$$

where

$$\boldsymbol{\Phi}_{\pm}=[X_{\pm}^{-N}\ X_{\pm}^{-N+1}\ \cdots\ X_{\pm}^{N-1}]^{\mathrm{T}}\ ,$$
$$\boldsymbol{H}_{\pm}=\begin{bmatrix} H_{\pm}^{-N,-N} & H_{\pm}^{-N,-N+1} & \cdots & H_{\pm}^{-N,N-1} \\ H_{\pm}^{-N+1,-N} & H_{\pm}^{-N+1,-N+1} & \cdots & H_{\pm}^{-N+1,N-1} \\ \cdot & \cdot & \cdots & \cdot \\ \cdot & \cdot & \cdots & \cdot \\ \cdot & \cdot & \cdots & \cdot \\ H_{\pm}^{N-1,-N} & H_{\pm}^{N-1,-N+1} & \cdots & H_{\pm}^{N-1,N-1} \end{bmatrix}. \tag{13}$$

$\boldsymbol{H}_{\pm}$ can easily be calculated by the Fast Fourier Transform.

Similarly, the condition for continuity of traction must be imposed along the interface. Taking $\boldsymbol{n}=(n_x, 0, n_z)$ as the unit normal to the interface (Fig. 2.2), we require continuity of the traction

$$\boldsymbol{T}=[T_x, T_y, T_z]\ ,$$
$$T_x=\tau_{xx}n_x+\tau_{xz}n_z$$

$$T_y=\tau_{xy}n_x+\tau_{zy}n_z$$
$$T_z=\tau_{zz}n_x+\tau_{zz}n_z\ . \tag{14}$$

From (4) we have

$$T_x=\lambda n_x\left(\frac{\partial u}{\partial x}+\frac{\partial w}{\partial z}\right)+\mu\left(2n_x\frac{\partial u}{\partial x}+n_z\left(\frac{\partial u}{\partial z}+\frac{\partial w}{\partial x}\right)\right)$$
$$T_z=\lambda n_z\left(\frac{\partial u}{\partial x}+\frac{\partial w}{\partial z}\right)+\mu\left(2n_z\frac{\partial w}{\partial z}+n_x\left(\frac{\partial u}{\partial z}+\frac{\partial w}{\partial x}\right)\right)$$
$$T_y=\mu\left(n_x\frac{\partial v}{\partial x}+n_z\frac{\partial v}{\partial z}\right)\ . \tag{15}$$

In $1-D$ media only the continuity of τ_{zx}, τ_{zz} and τ_{zy} is required, because $\boldsymbol{n}=(0, 0, 1)$. Moreover, it is good enough for $1-D$ media that transformed stresses individually satisfy these conditions as

$$\tilde{s}_1(k, z^0, \omega)=\tilde{s}_2(k, z^0, \omega)$$
$$\tilde{t}_1(k, z^0, \omega)=\tilde{t}_2(k, z^0, \omega)$$
$$\tilde{p}_1(k, z^0, \omega)=\tilde{p}_2(k, z^0, \omega)\ . \tag{16}$$

On the other hand, for irregular interfaces we should apply the same procedure to $\boldsymbol{T}$ as to the displacement. Using equations

$$n_x=\frac{-h'}{(1+h'^2)^{1/2}}\ ,\quad n_z=\frac{1}{(1+h'^2)^{1/2}}\ ,\quad h'=\frac{dh}{dx}\ ,$$

we obtain

$$\sum_{n=-N}^{N-1}\left[{}^x_PJ^{mn}_{1-P}X^n_{1-}+{}^x_PJ^{mn}_{1+P}X^n_{1+}+{}^x_VJ^{mn}_{1-V}X^n_{1-}+{}^x_VJ^{mn}_{1+V}X^n_{1+}\right]$$
$$=\sum_{n=-N}^{N-1}\left[{}^x_PJ^{mn}_{2-P}X^n_{2-}+{}^x_PJ^{mn}_{2+P}X^n_{2+}+{}^x_VJ^{mn}_{2-V}X^n_{2-}+{}^x_VJ^{mn}_{2+V}X^n_{2+}\right]$$
$$\sum_{n=-N}^{N-1}\left[{}^z_PJ^{mn}_{1-P}X^n_{1-}+{}^z_PJ^{mn}_{1+P}X^n_{1+}+{}^z_VJ^{mn}_{1-V}X^n_{1-}+{}^z_VJ^{mn}_{1+V}X^n_{1+}\right]$$
$$=\sum_{n=-N}^{N-1}\left[{}^z_PJ^{mn}_{2-P}X^n_{2-}+{}^z_PJ^{mn}_{2+P}X^n_{2+}+{}^z_VJ^{mn}_{2-V}X^n_{2-}+{}^z_VJ^{mn}_{2+V}X^n_{2+}\right]$$
$$\sum_{n=-N}^{N-1}\left[{}_HJ^{mn}_{1-H}X^n_{1-}+{}_HJ^{mn}_{1+H}X^n_{1+}\right]=\sum_{n=-N}^{N-1}\left[{}_HJ^{mn}_{2-H}X^n_{2-}+{}_HJ^{mn}_{2+H}X^n_{2+}\right]\ ,$$
$$m=-N,\ -N+1,\ \cdots,\ N-1$$
$$J^{mn}=\frac{\Delta k}{2\pi}\int_{-\infty}^{+\infty}J^n e^{j(n-m)\Delta kx}dx\ , \tag{17}$$

where

$${}^x_PJ^n_{\pm}=\frac{\mu}{(1+h'^2)^{1/2}}\left[-h'(2\nu^2_{\alpha n}-k^2_\beta)\pm 2n\Delta k\nu_{\alpha n}\right]e^{\mp j\nu_{\alpha n}h(x)}$$

$$
\begin{aligned}
{}^{x}_{V}J^{n}_{\pm} &= \frac{\mu}{(1+h'^2)^{1/2}}[\pm h'n\Delta k\nu_{\beta n} - l]e^{\mp i\nu_{\beta n}h(x)} \\
{}^{z}_{P}J^{n}_{\pm} &= \frac{\mu}{(1+h'^2)^{1/2}}[\mp h'n\Delta k\nu_{\alpha n} + l]e^{\mp j\nu_{\alpha n}h(x)} \\
{}^{z}_{V}J^{n}_{\pm} &= \frac{\mu}{(1+h'^2)^{1/2}}[h'l \pm 2n\Delta k\nu_{\beta n}]e^{\mp j\nu_{\beta n}h(x)} \\
{}_{H}J^{n}_{\pm} &= \frac{\mu}{(1+h'^2)^{1/2}}[-h'jn\Delta k \mp j\nu_{\beta n}]e^{\mp j\nu_{\alpha n}h(x)} \ , \qquad (18)
\end{aligned}
$$

with $l=2k^2-k_\beta^2$. Thus, the matrix form of the continuity condition for traction becomes

$$
\begin{bmatrix} {}^{x}_{P}\boldsymbol{J}_{1-} & {}^{x}_{V}\boldsymbol{J}_{1-} & {}^{x}_{P}\boldsymbol{J}_{1+} & {}^{x}_{V}\boldsymbol{J}_{1+} \\ {}^{z}_{P}\boldsymbol{J}_{1-} & {}^{z}_{V}\boldsymbol{J}_{1-} & {}^{z}_{P}\boldsymbol{J}_{1+} & {}^{z}_{V}\boldsymbol{J}_{1+} \end{bmatrix} \begin{bmatrix} {}_{P}\boldsymbol{\Phi}_{1-} \\ {}_{V}\boldsymbol{\Phi}_{1-} \\ {}_{P}\boldsymbol{\Phi}_{1+} \\ {}_{V}\boldsymbol{\Phi}_{1+} \end{bmatrix} = \begin{bmatrix} {}^{x}_{P}\boldsymbol{J}_{2-} & {}^{x}_{V}\boldsymbol{J}_{2-} & {}^{x}_{P}\boldsymbol{J}_{2+} & {}^{x}_{V}\boldsymbol{J}_{2+} \\ {}^{z}_{P}\boldsymbol{J}_{2-} & {}^{z}_{V}\boldsymbol{J}_{2-} & {}^{z}_{P}\boldsymbol{J}_{2+} & {}^{z}_{V}\boldsymbol{J}_{2+} \end{bmatrix} \begin{bmatrix} {}_{P}\boldsymbol{\Phi}_{2-} \\ {}_{V}\boldsymbol{\Phi}_{2-} \\ {}_{P}\boldsymbol{\Phi}_{2+} \\ {}_{V}\boldsymbol{\Phi}_{2+} \end{bmatrix}
$$

$$
[{}_{H}\boldsymbol{J}_{1-} \ \ {}_{H}\boldsymbol{J}_{1+}] \begin{bmatrix} {}_{H}\boldsymbol{\Phi}_{1-} \\ {}_{H}\boldsymbol{\Phi}_{1+} \end{bmatrix} = [{}_{H}\boldsymbol{J}_{2-} \ \ {}_{H}\boldsymbol{J}_{2+}] \begin{bmatrix} {}_{H}\boldsymbol{\Phi}_{2-} \\ {}_{H}\boldsymbol{\Phi}_{2+} \end{bmatrix} \qquad (19)
$$

where

$$
\boldsymbol{J}_{\pm} = \begin{bmatrix} J^{-N,-N}_{\pm} & J^{-N,-N+1}_{\pm} & \cdots & J^{-N,N-1}_{\pm} \\ J^{-N+1,-N}_{\pm} & J^{-N+1,-N+1}_{\pm} & \cdots & J^{-N+1,N-1}_{\pm} \\ \cdot & \cdot & \cdots & \cdot \\ \cdot & \cdot & \cdots & \cdot \\ \cdot & \cdot & \cdots & \cdot \\ J^{N-1,-N}_{\pm} & J^{N-1,-N+1}_{\pm} & \cdots & J^{N-1,N-1}_{\pm} \end{bmatrix} .
$$

Finally, by combining (19) with (12) the boundary conditions of the $P-SV$ wave at the irregular interface yield $8N$ linear equations with the $8N$ variables (${}_{P}X^{n}_{\pm}$ and ${}_{V}X^{n}_{\pm}$),

$$
\boldsymbol{K}_1\boldsymbol{\Phi}_1 = \boldsymbol{K}_2\boldsymbol{\Phi}_2 \qquad (20)
$$

where

$$
\boldsymbol{K} = \begin{bmatrix} {}^{x}_{P}\boldsymbol{H}_{-} & {}^{x}_{V}\boldsymbol{H}_{-} & {}^{x}_{P}\boldsymbol{H}_{+} & {}^{x}_{V}\boldsymbol{H}_{+} \\ {}^{z}_{P}\boldsymbol{H}_{-} & {}^{z}_{V}\boldsymbol{H}_{-} & {}^{z}_{P}\boldsymbol{H}_{+} & {}^{z}_{V}\boldsymbol{H}_{+} \\ {}^{x}_{P}\boldsymbol{J}_{-} & {}^{x}_{V}\boldsymbol{J}_{-} & {}^{x}_{P}\boldsymbol{J}_{+} & {}^{x}_{V}\boldsymbol{J}_{+} \\ {}^{z}_{P}\boldsymbol{J}_{-} & {}^{z}_{V}\boldsymbol{J}_{-} & {}^{z}_{P}\boldsymbol{J}_{+} & {}^{z}_{V}\boldsymbol{J}_{+} \end{bmatrix}
$$

$$
\boldsymbol{\Phi} = [{}_{P}\boldsymbol{\Phi}_{-} \ \ {}_{V}\boldsymbol{\Phi}_{-} \ \ {}_{P}\boldsymbol{\Phi}_{+} \ \ {}_{V}\boldsymbol{\Phi}_{+}]^{\mathrm{T}} .
$$

The conditions for the SH wave similarly yield $4N$ linear equations with $4N$ variables (${}_{H}X^{n}_{\pm}$), where

$$\boldsymbol{K}=\begin{bmatrix} {}_{H}\boldsymbol{H}_{-} & {}_{H}\boldsymbol{H}_{+} \\ {}_{H}\boldsymbol{J}_{-} & {}_{H}\boldsymbol{J}_{+} \end{bmatrix}$$
$$\boldsymbol{\Phi}=[{}_{H}\boldsymbol{\Phi}_{-}\ {}_{H}\boldsymbol{\Phi}_{+}]^{\mathrm{T}} . \tag{21}$$

$\boldsymbol{K}$, which represents scattering due to the irregular interface, will hereafter be called the *Irregularity Matrix.*

2. 2 Propagator matrix

Some vectors and matrices defined by HASKELL (1953) for individual wavenumbers are used in the reflectivity method developed for $1-D$ media. The motion-stress vector expressing the wave-field was defined for the wavenumber $n\Delta k$ as

$$\begin{aligned} \boldsymbol{s}^{n}(z)&=[\tilde{u}^{n}\ \tilde{v}^{n}\ \tilde{s}^{n}\ \tilde{t}^{n}]^{\mathrm{T}} \quad (P-SV) \\ &=[\tilde{v}^{n}\ \tilde{p}^{n}]^{\mathrm{T}} \qquad\qquad (SH) . \end{aligned} \tag{22}$$

Using this vector the boundary condition at a flat interface yields

$$\boldsymbol{s}_{1}^{n}(z^{0})=\boldsymbol{s}_{2}^{n}(z^{0}) . \tag{23}$$

The amplitude vector

$$\begin{aligned} \boldsymbol{\Phi}^{n}(z)&=[{}_{P}X_{-}^{n}\ {}_{V}X_{-}^{n}\ {}_{P}X_{+}^{n}\ {}_{V}X_{+}^{n}]^{\mathrm{T}} \quad (P-SV) \\ &=[{}_{H}X_{-}^{n}\ {}_{H}X_{+}^{n}]^{\mathrm{T}} \qquad\qquad (SH) \end{aligned} \tag{24}$$

was introduced to represent the solutions of the wave equation (7). These vectors are related by

$$\boldsymbol{s}^{n}(z)=\boldsymbol{t}^{n}\boldsymbol{\Phi}^{n}(z) , \tag{25}$$

$$\boldsymbol{t}^{n}=\begin{bmatrix} +jk & -j\nu_{\beta} & +jk & +j\nu_{\beta} \\ +j\nu_{\alpha} & +jk & -j\nu_{\alpha} & +jk \\ +\mu l & -2\mu k\nu_{\beta} & +\mu l & +2\mu k\nu_{\beta} \\ -2\mu k\nu_{\alpha} & -\mu l & +2\mu k\nu_{\alpha} & -\mu l \end{bmatrix} \quad (P-SV)$$

$$=\begin{bmatrix} 1 & 1 \\ +j\mu\nu_{\beta n} & -j\mu\nu_{\beta n} \end{bmatrix} \qquad (SH) .$$

Two amplitude vectors at different depths in a layer are also related by

$$\boldsymbol{\Phi}^{n}(z+d)=\boldsymbol{e}^{n}(d)\boldsymbol{\Phi}^{n}(z) \tag{26}$$

in which:

$$\boldsymbol{e}^{n}(d)=\begin{bmatrix} e^{+j\nu_{\alpha n}d} & 0 & 0 & 0 \\ 0 & e^{+j\nu_{\beta n}d} & 0 & 0 \\ 0 & 0 & e^{-j\nu_{\alpha n}d} & 0 \\ 0 & 0 & 0 & e^{-j\nu_{\beta n}d} \end{bmatrix} \quad (P-SV)$$

$$=\begin{bmatrix} e^{+j\nu_{\beta n}z} & 0 \\ 0 & e^{-j\nu_{\beta n}z} \end{bmatrix} \qquad (SH)\ .$$

Then we can relate two motion-stress vectors at different depths in a layer as

$$\begin{aligned} \boldsymbol{s}^n(z+d)&=\boldsymbol{g}^n(d)\boldsymbol{s}^n(z) \\ \boldsymbol{g}^n(d)&=\boldsymbol{t}^n\boldsymbol{e}^n(d)\boldsymbol{t}^{n-1}\ . \end{aligned} \tag{27}$$

$\boldsymbol{g}^n$ is usually called a *Propagator Matrix*. We now specify these matrices for the k-th layer with $\boldsymbol{g}_k^n=\boldsymbol{g}^n(d_k)$, $\boldsymbol{t}_k^n$ and $\boldsymbol{e}_k^n=\boldsymbol{e}^n(d_k)$, and the vectors with $\boldsymbol{s}_k^n(z)$ and $\boldsymbol{\Phi}_k^n$. Using the propagator matrices and the boundary condition (23) for $1-D$ media, the motion-stress vector $\boldsymbol{s}_1^n(z_0^0)$ at the free surface is related to the amplitude vector $\boldsymbol{\Phi}_M^n(z_{M-1}^0)$ at the upper boundary of the halfspace by

$$\begin{aligned} \boldsymbol{\Phi}_M^n(z_{M-1}^0)&=\boldsymbol{m}^n\boldsymbol{s}_1^n(z_0^0)\ , \\ \boldsymbol{m}^n&=\boldsymbol{t}_M^{n-1}\boldsymbol{g}_{M-1}^n\boldsymbol{g}_{M-2}^n\cdots\boldsymbol{g}_1^n\ . \end{aligned} \tag{28}$$

If we apply the stress free condition and the radiation condition

$$\begin{aligned} \boldsymbol{s}_1^n(z_0^0)&=[U^n\ \ W^n\ \ 0\ \ 0]^{\mathrm{T}} \quad \text{or} \quad [V^n\ \ 0]^{\mathrm{T}} \\ \boldsymbol{\Phi}_M^n(z_{M-1}^0)&=[0\ \ 0\ \ {}_PX_{M+}^n\ \ {}_VX_{M+}^n]^{\mathrm{T}} \quad \text{or} \quad [0\ \ {}_HX_{M+}^n]^{\mathrm{T}} \end{aligned} \tag{29}$$

to (28), we can obtain transformed surface displacements U^n, W^n and V^n for $1-D$ media. Synthetic seismograms computed from these transforms are complete, because there is no approximation in our formulation.

On the other hand, the boundary conditions at irregular interfaces cannot be satisfied for individual wavenumbers, but only for the total wave-field as shown in the preceding section. Thus the reflectivity method itself should be modified to treat it. When we consider wavenumbers from $-N\Delta k$ to $(N-1)\Delta k$, the total wave-field can be expressed by the enlarged motion-stress vector

$$\begin{aligned} \boldsymbol{S}(z)&=[\boldsymbol{u}\ \ \boldsymbol{w}\ \ \boldsymbol{s}\ \ \boldsymbol{t}]^{\mathrm{T}} \quad (P-SV) \\ &=[\boldsymbol{v}\ \ \boldsymbol{p}]^{\mathrm{T}} \qquad (SH) \\ \boldsymbol{u}&=[\tilde{u}^{-N}\ \ \tilde{u}^{-N+1}\cdots\tilde{u}^{N-1}]^{\mathrm{T}} \\ \boldsymbol{w}&=[\tilde{w}^{-N}\ \ \tilde{w}^{-N+1}\cdots\tilde{w}^{N-1}]^{\mathrm{T}} \\ \boldsymbol{v}&=[\tilde{v}^{-N}\ \ \tilde{v}^{-N+1}\cdots\tilde{v}^{N-1}]^{\mathrm{T}} \\ \boldsymbol{s}&=[\tilde{s}^{-N}\ \ \tilde{s}^{-N+1}\cdots\tilde{s}^{N-1}]^{\mathrm{T}} \\ \boldsymbol{t}&=[\tilde{t}^{-N}\ \ \tilde{t}^{-N+1}\cdots\tilde{t}^{N-1}]^{\mathrm{T}} \\ \boldsymbol{p}&=[\tilde{p}^{-N}\ \ \tilde{p}^{-N+1}\cdots\tilde{p}^{N-1}]^{\mathrm{T}}\ , \end{aligned} \tag{30}$$

where $\tilde{u}^n=\tilde{u}(n\Delta k, z, \omega)$ *etc.* We can also define the enlarged propagator

matrix $\boldsymbol{G}(d)$ for this vector as

$$\boldsymbol{G}(d)=\begin{bmatrix}\boldsymbol{G}_{11} & \boldsymbol{G}_{12} & \boldsymbol{G}_{13} & \boldsymbol{G}_{14}\\ \boldsymbol{G}_{21} & \boldsymbol{G}_{22} & \boldsymbol{G}_{23} & \boldsymbol{G}_{24}\\ \boldsymbol{G}_{31} & \boldsymbol{G}_{32} & \boldsymbol{G}_{33} & \boldsymbol{G}_{34}\\ \boldsymbol{G}_{41} & \boldsymbol{G}_{42} & \boldsymbol{G}_{43} & \boldsymbol{G}_{44}\end{bmatrix} \quad (P-SV)$$

$$=\begin{bmatrix}\boldsymbol{G}_{11} & \boldsymbol{G}_{12}\\ \boldsymbol{G}_{21} & \boldsymbol{G}_{22}\end{bmatrix} \quad (SH) \tag{31}$$

$$\boldsymbol{G}_{ij}=\begin{bmatrix} g_{ij}^{-N} & & & & \\ & g_{ij}^{-N+1} & & & \\ & & \cdot & & \\ & & & \cdot & \\ & & & & \cdot \\ & & & & g_{ij}^{N-1}\end{bmatrix}.$$

$\boldsymbol{G}(d)$ consists of sixteen or four diagonal submatrices. A submatrix $\boldsymbol{G}_{ij}$ further consists of the (i, j) elements of the propagator matrices $\boldsymbol{g}^{-N}$, $\boldsymbol{g}^{-N+1}$, $\cdots$, $\boldsymbol{g}^{N-1}$. Like $\boldsymbol{g}^n(d)$, $\boldsymbol{G}(d)$ can also be factored as

$$\boldsymbol{G}(d)=\boldsymbol{T}\boldsymbol{E}(d)\boldsymbol{T}^{-1}. \tag{32}$$

$\boldsymbol{T}$ and $\boldsymbol{E}(d)$ have such a partitioned diagonal form as $\boldsymbol{G}(d)$. Their submatrices are made of the elements of $\boldsymbol{t}$ and $\boldsymbol{e}(d)$. After some matrix calculations we find that $\boldsymbol{T}^{-1}$ is a partitioned diagonal matrix consisting of the elements of $\boldsymbol{t}^{-1}$.

We again specify these enlarged matrices for the k-th layer with $\boldsymbol{G}_k=\boldsymbol{G}(d_k)$, $\boldsymbol{T}_k$ and $\boldsymbol{E}_k=\boldsymbol{E}(d_k)$, and the enlarged motion-stress vector with $\boldsymbol{S}_k(z)$. The following relations among them are still valid:

$$\begin{aligned}&\boldsymbol{S}_k(z_k^0)=\boldsymbol{G}_k\boldsymbol{S}_k(z_{k-1}^0)\\ &\boldsymbol{S}_k(z)=\boldsymbol{T}_k\boldsymbol{\Phi}_k(z)\,,\end{aligned} \tag{33}$$

where $\boldsymbol{\Phi}_k$ is the enlarged amplitude vector defined for the k-th layer by (20) and (21). The condition of continuity at the k-th flat interface and the stress-free condition at the flat surface are simply represented as

$$\begin{aligned}&\boldsymbol{S}_k(z_k^0)=\boldsymbol{S}_{k+1}(z_k^0)\\ &\boldsymbol{S}_1(z_0^0)=[U\ \ W\ 0\ \ 0]^{\mathrm{T}} \quad (P-SV)\\ &\qquad\quad =[V\ 0]^{\mathrm{T}} \qquad\quad (SH)\end{aligned} \tag{34}$$

with

$$\begin{aligned}U&=[U^{-N}\ \ U^{-N+1}\cdots U^{N-1}]^{\mathrm{T}}\\ W&=[W^{-N}\ \ W^{-N+1}\cdots W^{N-1}]^{\mathrm{T}}\end{aligned}$$

$$V=[V^{-N}\ V^{-N+1}\cdots V^{N-1}]^{\mathrm{T}}$$
$$\mathbf{0}=[0\ 0\cdots 0]^{\mathrm{T}}\ .$$

For the irregular interface, on the other hand, we have

$$\boldsymbol{K}_{k,k}\boldsymbol{\Phi}_k(z_k^0)=\boldsymbol{K}_{k,k+1}\boldsymbol{\Phi}_{k+1}(z_k^0) \tag{35}$$

from (20). $\boldsymbol{K}_{i,j}$ is the irregularity matrix for the i-th interface on the side of the j-th layer. Inserting (33) into (35) the condition for the enlarged motion-stree vector can be written as

$$\boldsymbol{K}_{k,k}\boldsymbol{T}_k^{-1}\boldsymbol{S}_k(z_k^0)=\boldsymbol{K}_{k,k+1}\boldsymbol{T}_{k+1}^{-1}\boldsymbol{S}_{k+1}(z_k^0)\ . \tag{36}$$

Similarly, at the irregular surface we have the stress-free condition

$$\boldsymbol{K}_{0,1}\boldsymbol{T}_1^{-1}\boldsymbol{S}_1(z_0^0)=[U\ \ W\ 0\ 0]^{\mathrm{T}}\quad\text{or}\quad[V\ 0]^{\mathrm{T}}\ . \tag{37}$$

$1-D$ and $2-D$ media have the same radiation condition

$$\boldsymbol{\Phi}_M(z_{M-1}^0)=[0\ 0\ {}_P\Phi_{M+}\ {}_V\Phi_{M+}]^{\mathrm{T}}\quad\text{or}\quad[0\ {}_H\Phi_{M+}]^{\mathrm{T}} \tag{38}$$

in the total wave-field.

Now we can carry the total wave-field in the halfspace up to the free surface using the boundary conditions (34) or (36). When all the interfaces are flat, the motion-stress vector $\boldsymbol{S}_1(z_0^0)$ is related to $\boldsymbol{\Phi}_M(z_{M-1}^0)$ by

$$\boldsymbol{\Phi}_M(z_{M-1}^0)=\boldsymbol{M}\boldsymbol{S}_1(z_0^0)\ ,$$
$$\boldsymbol{M}=\boldsymbol{T}_M^{-1}\boldsymbol{G}_{M-1}\boldsymbol{G}_{M-2}\cdots\boldsymbol{G}_1\ . \tag{39}$$

This equation is identical to (28), which was derived for an individual wave-field, excepting the enlarged form of the matrices. If only the k-th interface is irregular and all of the others are flat, $\boldsymbol{M}$ in (39) becomes

$$\boldsymbol{M}=\boldsymbol{T}_M^{-1}\boldsymbol{G}_{M-1}\boldsymbol{G}_{M-2}\cdots\boldsymbol{G}_{k+1}\underline{\boldsymbol{T}_{k+1}\boldsymbol{K}_{k,k+1}^{-1}\boldsymbol{K}_{k,k}\boldsymbol{T}_k^{-1}}\boldsymbol{G}_k\boldsymbol{G}_{k-1}\cdots\boldsymbol{G}_1\ . \tag{40}$$

(40) is obtained by adding the part indicated with a underline to (39). In the case of an irregular surface we have

$$\boldsymbol{M}=\boldsymbol{T}_M^{-1}\boldsymbol{G}_{M-1}\boldsymbol{G}_{M-2}\cdots\boldsymbol{G}_{k+1}\underline{\boldsymbol{T}_{k+1}\boldsymbol{K}_{k,k+1}^{-1}\boldsymbol{K}_{k,k}\boldsymbol{T}_k^{-1}}\boldsymbol{G}_k\boldsymbol{G}_{k-1}\cdots\boldsymbol{G}_1\underline{\boldsymbol{T}_1\boldsymbol{K}_{0,1}^{-1}} \tag{41}$$

from (37). Furthermore, if all of the interfaces and the surface are irregular, (41) yields

$$\boldsymbol{M}=\boldsymbol{K}_{M-1,M}^{-1}\boldsymbol{K}_{M-1,M-1}\boldsymbol{E}_{M-1}\boldsymbol{K}_{M-2,M-1}^{-1}\boldsymbol{K}_{M-2.M-2}\boldsymbol{E}_{M-2}\cdots\boldsymbol{K}_{1,2}^{-1}\boldsymbol{K}_{1,1}\boldsymbol{E}_1\boldsymbol{K}_{1,0}^{-1} \tag{42}$$

by (32).

2. 3 Synthetic seismogram

In this section we will show how to compute synthetic seismograms using the boundary conditions and the enlarged propagator matrices

presented in the previous section. Seismograms due to a plane wave, a line force and a point dislocation will be considered.

(1) Plane wave incidence

Hereafter we drop "enlarged" from terms such as the enlarged propagator matrix, the enlarged motion-stress vector *etc.* When a plane wave with the horizontal wavenumber $I\Delta k$ travels from the halfspace into the overlaying layers at time $t=0$, the radiation condition is slightly different from (38). If a plane P-wave is incident, the amplitude vector at the upper boundary of the halfspace is expressed as

$$\boldsymbol{\Phi}_M(z^0_{M-1})=[1\ \ 0\ \ {}_P\boldsymbol{\Phi}_{M+}\ \ {}_V\boldsymbol{\Phi}_{M+}]^{\mathrm{T}} \tag{43}$$

with

$$\mathbf{1}=[0\ \ 0\cdots 0\ \ 1\ \ 0\cdots 0]^{\mathrm{T}}\ .$$

In case of an incident SH-wave, it yields

$$\boldsymbol{\Phi}_M(z^0_{M-1})=[1\ \ {}_H\boldsymbol{\Phi}_{M+}]^{\mathrm{T}}\ . \tag{44}$$

Substituting (43), (44) and (34) for $\boldsymbol{\Phi}_M(z^0_{M-1})$ and $\boldsymbol{S}_1(z^0_0)$ in (39) we obtain

$$\begin{bmatrix} \mathbf{1} \\ \mathbf{0} \\ {}_P\boldsymbol{\Phi}_{M+} \\ {}_V\boldsymbol{\Phi}_{M+} \end{bmatrix} = \boldsymbol{M} \begin{bmatrix} \boldsymbol{U} \\ \boldsymbol{W} \\ \mathbf{0} \\ \mathbf{0} \end{bmatrix}$$

$$\begin{bmatrix} \mathbf{1} \\ {}_H\boldsymbol{\Phi}_{M+} \end{bmatrix} = \boldsymbol{M} \begin{bmatrix} \boldsymbol{V} \\ \mathbf{0} \end{bmatrix}. \tag{45}$$

Solving (45) for $\boldsymbol{U}$, $\boldsymbol{W}$ and $\boldsymbol{V}$ yields

$$\begin{aligned} \boldsymbol{U} &= (\boldsymbol{M}_{11}-\boldsymbol{M}_{12}\boldsymbol{M}_{22}^{-1}\boldsymbol{M}_{21})^{-1}\cdot\mathbf{1} \\ \boldsymbol{W} &= (\boldsymbol{M}_{12}-\boldsymbol{M}_{11}\boldsymbol{M}_{21}^{-1}\boldsymbol{M}_{22})^{-1}\cdot\mathbf{1} \\ \boldsymbol{V} &= \boldsymbol{M}_{11}^{-1}\cdot\mathbf{1} \end{aligned} \tag{46}$$

with the submatrices of $\boldsymbol{M}$ defined as

$$\boldsymbol{M}=\begin{bmatrix} \boldsymbol{M}_{11} & \boldsymbol{M}_{12} & \boldsymbol{M}_{13} & \boldsymbol{M}_{14} \\ \boldsymbol{M}_{21} & \boldsymbol{M}_{22} & \boldsymbol{M}_{23} & \boldsymbol{M}_{24} \\ \boldsymbol{M}_{31} & \boldsymbol{M}_{32} & \boldsymbol{M}_{33} & \boldsymbol{M}_{34} \\ \boldsymbol{M}_{41} & \boldsymbol{M}_{42} & \boldsymbol{M}_{43} & \boldsymbol{M}_{44} \end{bmatrix} \quad \text{or} \quad \begin{bmatrix} \boldsymbol{M}_{11} & \boldsymbol{M}_{12} \\ \boldsymbol{M}_{21} & \boldsymbol{M}_{22} \end{bmatrix}. \tag{47}$$

The surface displacement can be obtained by integrating numerically the elements of $\boldsymbol{U}$, $\boldsymbol{W}$ and $\boldsymbol{V}$ and inverting the integral into the time domain with FFT.

Since there are surface wave poles along the integration path (the

real k axis), some of the elements diverge to infinity. In order to avoid this mathematical difficulty, we introduce a small imaginary part into frequencies as $\omega=\omega_R-j\omega_I$. It moves all the poles away from the real axis into the second and fourth quadrants of the complex k plane. It also prevents aliasing in the time domain. Its effect can easily be removed from the final time history by multiplying $e^{\omega_I t}$. For all the computations in this paper we will take $\omega_I=\pi/T$ (T; duration of seismogram).

Here we test the validity of our method against other techniques such as the Aki-Larner method (**AL**, BARD and BOUCHON 1980), the asymptotic ray theory (**ART**, HONG and HELMBERGER 1978), the Gaussian beam method (**GB**, NOWACK and AKI 1984), the finite difference method (**FD**, BOORE *et al.* 1971), or the finite element method (**FE**, HONG and KOSLOFF 1978). *SH* waves in the basin structure of Fig. 2.3 have already been studied with these methods. The symmetrical basin varies in thickness from 1 km at the edge to 6 km in the center along the interface

$$z(x)=D+\frac{C}{2}\left[1-\cos\left(2\pi\left(x-\frac{w}{2}\right)\Big/w\right)\right], \tag{48}$$

$$w=50\text{ km}\ ,\quad D=1\text{ km}\ ,\quad C=5\text{ km}\ .$$

A plane *SH* wave is impinging vertically from the lower halfspace. Its time function (Fig. 2.4) is described by the Ricker function

$$f(t)=\frac{\sqrt{\pi}}{2}\left(b^2-\frac{1}{2}\right)e^{-b^2} \tag{49}$$

where $b=\pi(t-t_s)/t_p$, $t_s=20$ sec and $t_p=18.3$ sec. Figure 2.5, in which our results are appended to Fig. 13.26 of AKI and RICHARDS (1980) and Fig. 19 of NOWACK and AKI (1984), compares synthetic seismograms generated by the six different methods. The letters at the tail of the rightmost traces indicate which method was used to compute them.

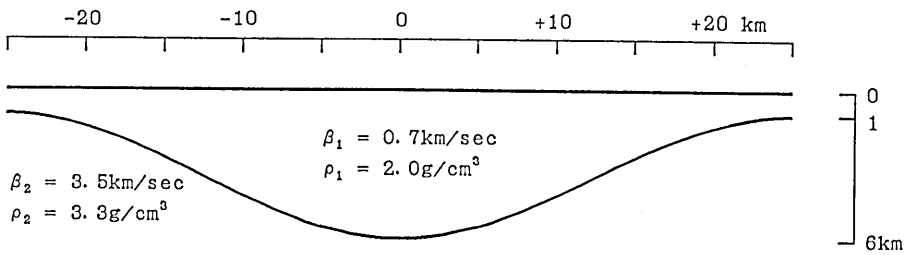

Fig. 2.3. A two-dimensional basin structure with a soft sediment layer. A plane *SH* wave is impinging vertically from the lower halfspace.

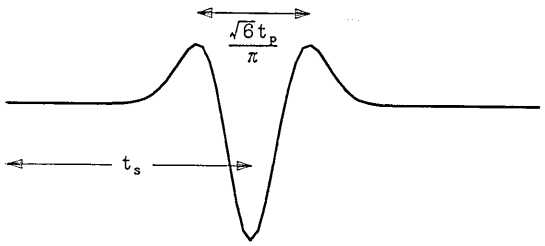

Fig. 2.4. Ricker's wavelet used as a source time function.

On computing our seismograms **RF**, we calculate the irregularity matrix **K** with $N=128$ and $\Delta k=2\pi/128$ km. If we directly apply the radiation condition of the halfspace at the irregular interface, up-going scattered waves will be neglected (AKI and RICHARDS 1980). To avoid this Rayleigh ansatz error, a dummy layer with material parameters identical to the halfspace is introduced immediately below the interface. The wave-field in the layer has an up-going part as shown in (7), and up-going waves scattered around the interface can be taken into account. Since our formulation has been constructed for multilayered media, we can easily insert layers at any depth. In all computations hereafter, a dummy layer will always be inserted.

Although the Aki-Larner method suffers the Rayleigh ansatz error,

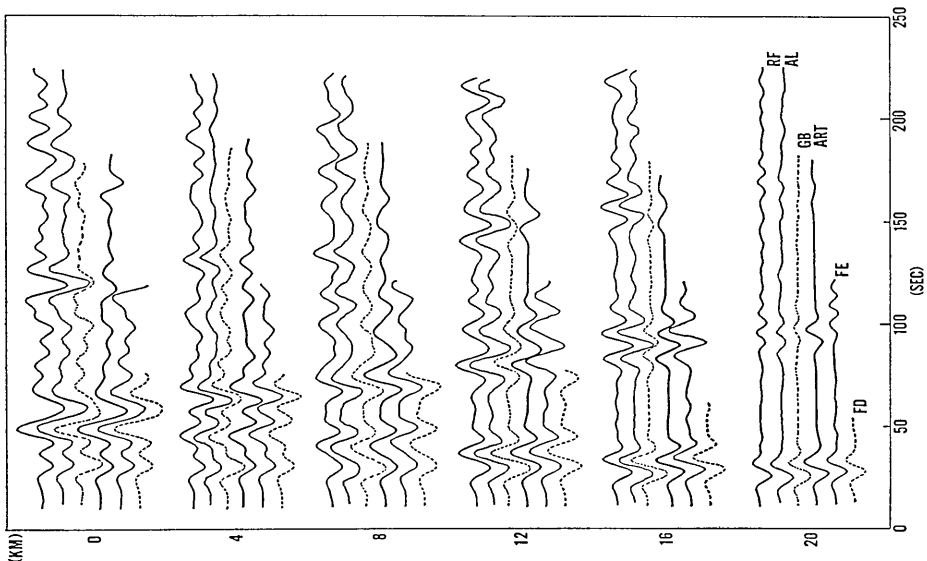

Fig. 2.5. Comparison of synthetic seismograms computed by various methods for motion on the surface of the structure in Fig. 2.3. Our seismograms are indicated by the letters **RF**. The results of Aki-Larner (**AL**), Gaussian Beam (**GB**), Asymptotic Ray Theory (**ART**), Finite Element (**FE**), and Finite Difference (**FD**) were obtained from AKI and RICHARDS (1980, Fig. 13.26), and NOWACK and AKI (1984, Fig. 19).

the seismograms **AL** of BARD and BOUCHON (1980) agree well with ours. This agreement shows that the error is small for the structure of Fig. 3 and the time function (37). In the lower halfspace, plane waves with (37) have a predominant wavelength of 64 km, which is sufficiently longer than the amplitude of interface irregularity, C.

In the early portion all of the traces agree with one another, but in the later portion the ray and beam seismograms (**ART** and **GB**) differ from the others. This may be due to the high-frequency feature of the asymptotic ray and beam theories, or to the neglect of some multiples in the seismograms.

As in the case of an irregular surface, we consider a simple mountain-like topography shown in Fig. 2.6. The S-wave velocity of the medium is 500 m/sec, and the time function of an incident SH wave is expressed by (49) with $t_p=0.2$ sec. The seismograms section in the left half of Fig. 2.7 was computed by BOORE (1972) with the finite difference method. He used the surface indicated in Fig. 2.6 by a solid line. Its ramp nature resulted from the grid configuration of his method. Since the wave length of the incident wave is sufficiently longer than the ramp size, we adopt the smooth surface indicated by a dashed line in computing our section in the right half. We take $N=64$ and $\Delta k=2\pi/128$ m for the irregularity matrix. The two sections excellently agree to each other. We find a strong amplification in the traces at the top of the mountain and a reflected wave from the other side in the traces at the mountain's foot.

We next consider the basin structure of Fig. 2.8, which consists of two layers. The upper and lower interfaces are expressed by (48)

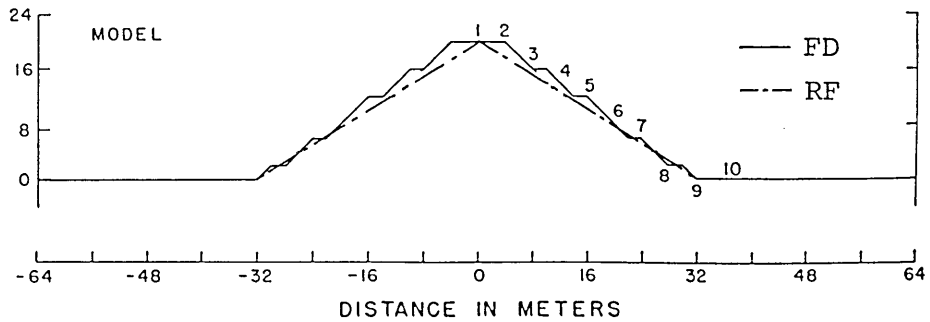

(after Boore,1972)

Fig. 2.6. A two-dimensional mountain-like structure. The solid line with ramp nature shows the surface used in the finite difference calculation. A plane SH wave is impinging vertically from the lower part.

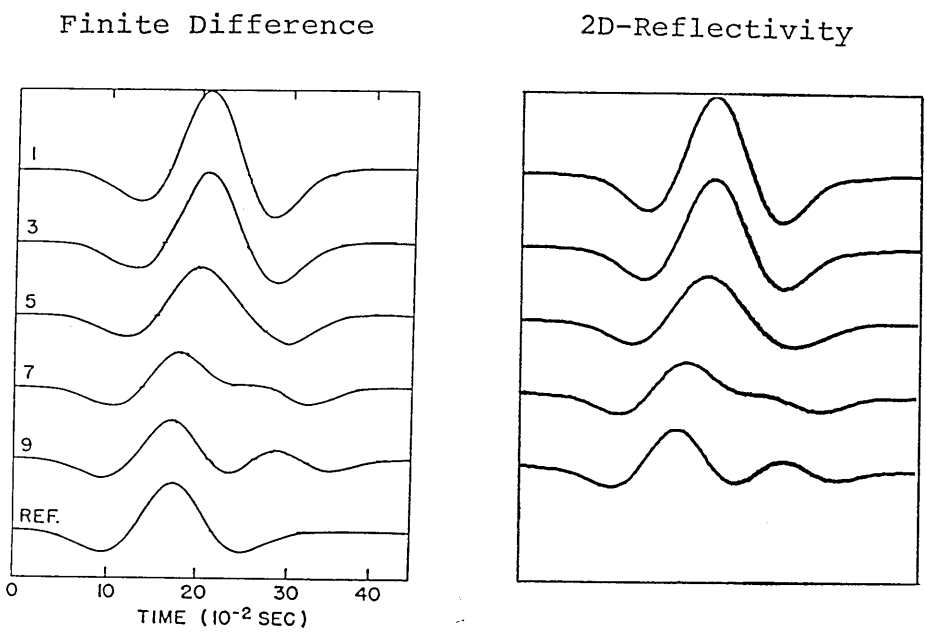

(after Boore, 1972)

Fig. 2.7. Comparison of synthetic seismograms computed for the model of Fig. 2.6 by the finite difference method and the $2-D$ reflectivity method. The numbers at the head of the left traces indicate for which point in Fig. 2.6 a trace is computed. The trace with letters **REF** is an input signal.

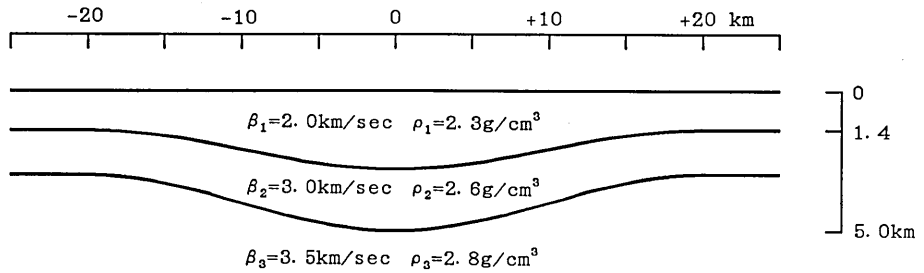

Fig. 2.8. A two-dimensional basin structure with two layers. The velocity contrast between the basin and the halfspace is rather low. A plane *SH* wave is impinging vertically from the lower halfspace.

with $(w, D, C)=(40\,\text{km}, 1.4\,\text{km}, 1.4\,\text{km})$ and $(40\,\text{km}, 3\,\text{km}, 2\,\text{km})$ respectively. The velocity contrast between the basin and the halfspace is rather low. Figure 2.9 compares our seismograms **RF** with the seismograms **FE** computed by Iwashita (personal communication) with

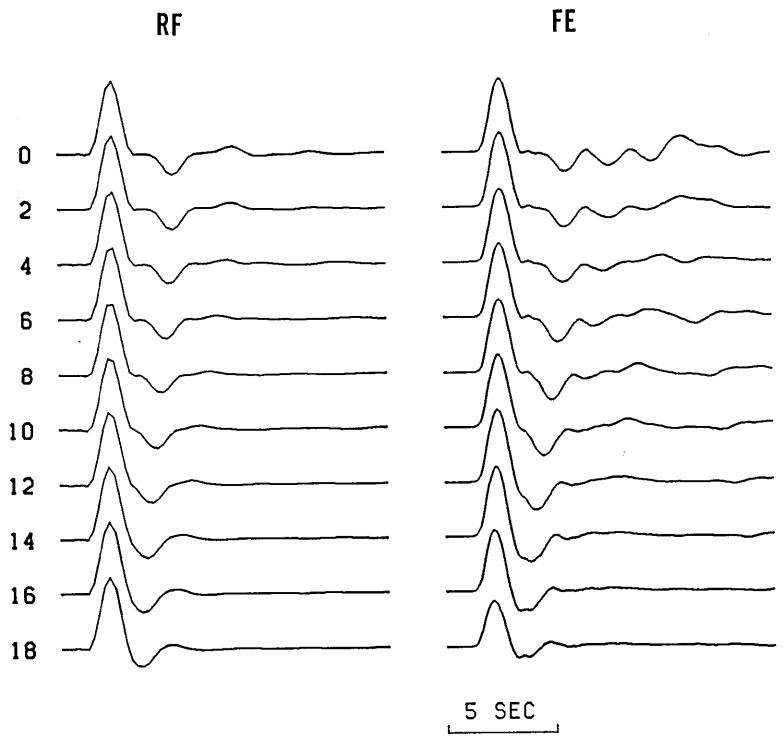

Fig. 2.9. Comparison of synthetic seismograms computed for the model of Fig. 2.8 by the $2-D$ reflectivity method (**RF**) and the finite element method (**FE**).

the finite element method. An incident SH wave has the time function

$$f(t)=(1-\cos 2\pi f_0 t)/2\pi f_0 \tag{50}$$

with $f_0=0.5$ Hz. In Fig. 2.9 we find two obvious differences. First the **FE** trace at 18 km has a much smaller amplitude than the **RF** trace. Secondly the **FE** traces close to the center of the basin are contaminated by some artificial phases in the later portion. In order to suppress artificial reflected waves due to the limit of model size, the efficient absorbing boundary of CUNDALL *et al.* (1978) was introduced at ± 20 km in the finite element computation. It suppressed actual waves as well as the artificial ones in its vicinity, and reduced the amplitude of the 18 km trace. Moreover, it could not perfectly erase artificial waves, which are distinct in the traces close to the basin center.

The last example in this part is presented to show the seismic response of a sedimentary basin due to an incident P wave. The basin

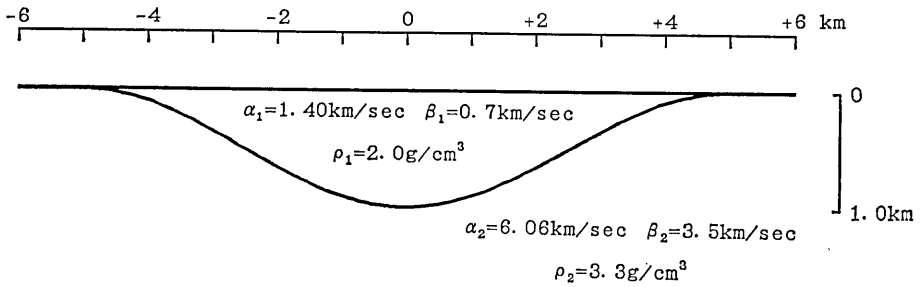

Fig. 2.10. A two-dimensional basin structure with a high velocity contrast. A plane P wave is impinging vertically from the lower halfspace.

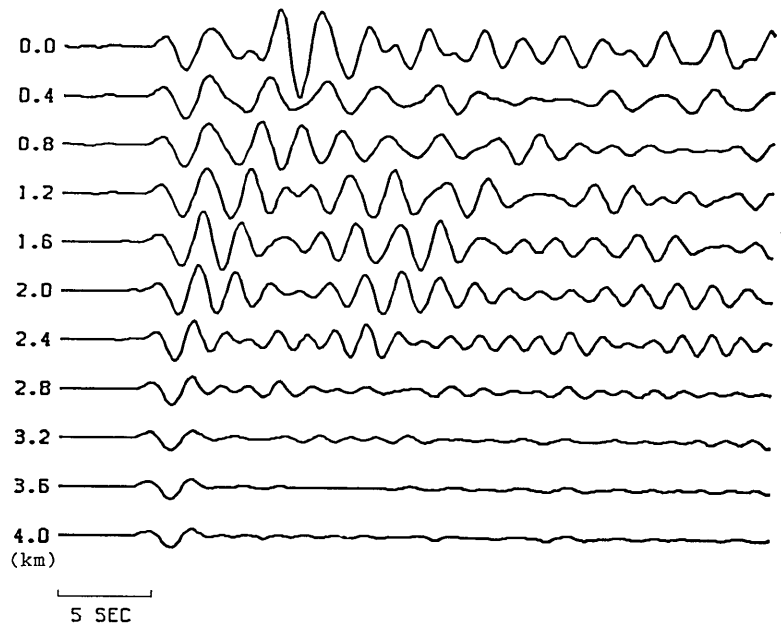

Fig. 2.11. Vertical responses of the model in Fig. 2.10 to an incident P wave.

shape in Fig. 2.10 is again represented by (48) with $w=10$ km, $D=0$ km and $C=1$ km. The Ricker's function (49) is also used with $t_p=2.8$ sec as a time function of the incident wave. We take $N=128$ and $\Delta k=2\pi/64$ km for the irregularity matrix. Fig. 2.11 shows vertical displacements at the free surface. Since the velocity contrast between the basin and the halfspace is as high as in the model of Fig. 2.3, a reverberation appears in the basin with large amplitudes.

(2) **Line source**

A buried line source requires somewhat different matrix calcula-

tions. The source causes discontinuity of displacement and stress represented by the discontinuity vector

$$\begin{aligned}
\Delta &= [\delta u \ \delta w \ \delta s \ \delta t]^{\mathrm{T}} \quad (P-SV) \\
&= [\delta v \ \delta p]^{\mathrm{T}} \quad (SH) \qquad (51) \\
\delta u &= [\delta \tilde{u}^{-N} \ \delta \tilde{u}^{-N+1} \cdots \delta \tilde{u}^{N-1}]^{\mathrm{T}} \\
\delta w &= [\delta \tilde{w}^{-N} \ \delta \tilde{w}^{-N+1} \cdots \delta \tilde{w}^{N-1}]^{\mathrm{T}} \\
\delta v &= [\delta \tilde{v}^{-N} \ \delta \tilde{v}^{-N+1} \cdots \delta \tilde{v}^{N-1}]^{\mathrm{T}} \\
\delta s &= [\delta \tilde{s}^{-N} \ \delta \tilde{s}^{-N+1} \cdots \delta \tilde{s}^{N-1}]^{\mathrm{T}} \\
\delta t &= [\delta \tilde{t}^{-N} \ \delta \tilde{t}^{-N+1} \cdots \delta \tilde{t}^{N-1}]^{\mathrm{T}} \\
\delta p &= [\delta \tilde{p}^{-N} \ \delta \tilde{p}^{-N+1} \cdots \delta \tilde{p}^{N-1}]^{\mathrm{T}} ,
\end{aligned}$$

where $\delta \tilde{u}^n = \delta \tilde{u}(n\Delta k, z, \omega)$ *etc.* We assume without loss of generality that the source is located on the s-th interface. As there is no incident wave from the halfspace, we have

$$\begin{aligned}
\begin{bmatrix} 0 \\ 0 \\ {}_P\Phi_{M+} \\ {}_V\Phi_{M+} \end{bmatrix} &= M_h \left[\Delta + M_l \begin{bmatrix} U \\ W \\ 0 \\ 0 \end{bmatrix} \right] \quad (P-SV) \\
\begin{bmatrix} 0 \\ {}_H\Phi_{M+} \end{bmatrix} &= M_h \left[\Delta + M_l \begin{bmatrix} V \\ 0 \end{bmatrix} \right] \quad (SH) \qquad (52)
\end{aligned}$$

instead of (45). The s-th interface divides M into the lower part M_h and the upper M_l. The solution of (52) is

$$\begin{aligned}
\begin{bmatrix} R_{11} & U \\ -R_{11} & W \end{bmatrix} &= \begin{bmatrix} -R_{11} & 0 & R_{13} & R_{15} \\ 0 & R_{11} & R_{12} & R_{13} \end{bmatrix} M_l^{-1} \Delta \\
-M_{11} \quad V \quad &= [M_{11} \ M_{12}] M_l^{-1} \Delta \qquad (53)
\end{aligned}$$

where

$$R_{st} = M_{jl} M_{km} - M_{jm} M_{kl} .$$

s, t (the subscripts of R)$=1, 2, 3, 4, 5, 6$ correspond to the pairs jk, lm (the subscripts of M)$=12, 13, 14, 23, 24, 34$. Like the plane wave incident problem the surface displacement due to the line source can be obtained by integrating numerically the elements of U, W and V and inverting the integral into the time domain.

We compute a section of seismograms with our $2-D$ reflectivity method for the flat two-layer (one layer and halfspace) structure where $\beta_1, \beta_2 = 2.0, 3.6\ \mathrm{km \cdot sec^{-1}}$ and $\rho_1, \rho_2 = 2.3, 2.8\ \mathrm{g \cdot cm^{-3}}$. A transverse line force is buried at 0.5 km depth in the upper layer 3 km thick. Figure 2.12 compares our section with the one computed by the $1-D$ reflec-

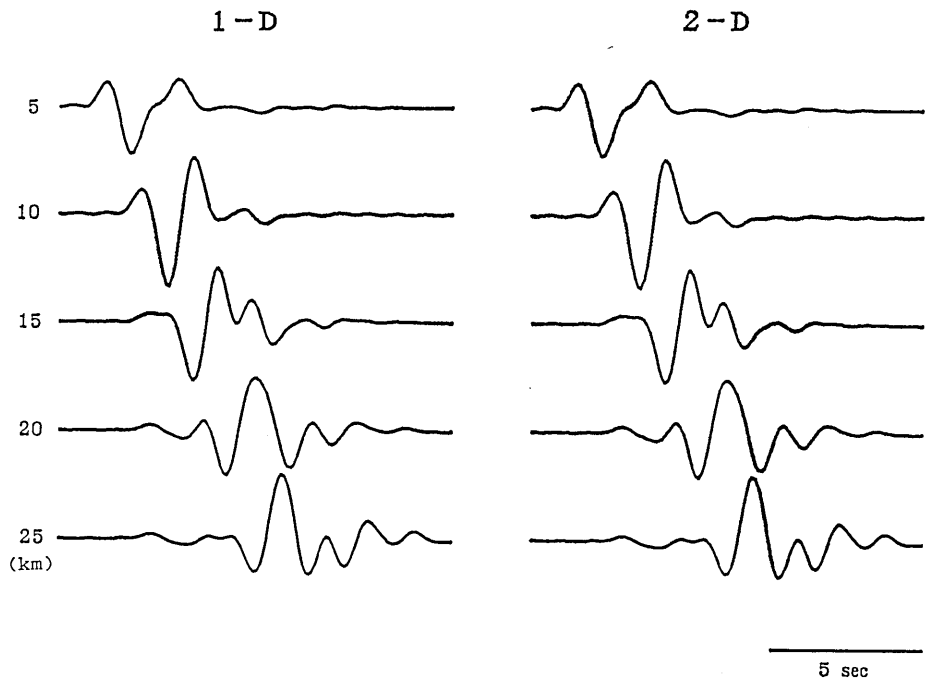

Fig. 2.12. Comparison of synthetic seismograms computed by the $1-D$ and $2-D$ reflectivity methods. The traces are tangential surface displacements at distances 5, 10, 20 and 25 km from a line force buried in a flat structure.

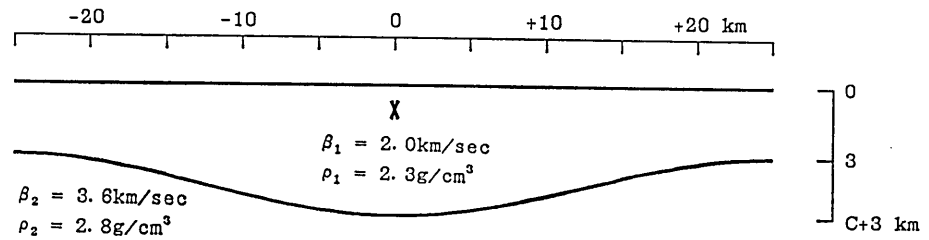

Fig. 2.13. A two-dimensionally irregular structure with a moderate velocity contrast. A line or point source is buried in the center of the upper basin.

tivity method. Their travel times are reduced with the velocity of the halfspace, 3.6 km/sec. As a source time function (49) is used with $t_p=1.83$ sec. The agreement between the two sections shows the validity of the $2-D$ reflectivity method for line source problems.

We next consider the basin structure shown in Fig. 2.13. In this structure the layer and the halfspace in the previous example are separated by the interface whose shape is expressed by (48) with $w=$

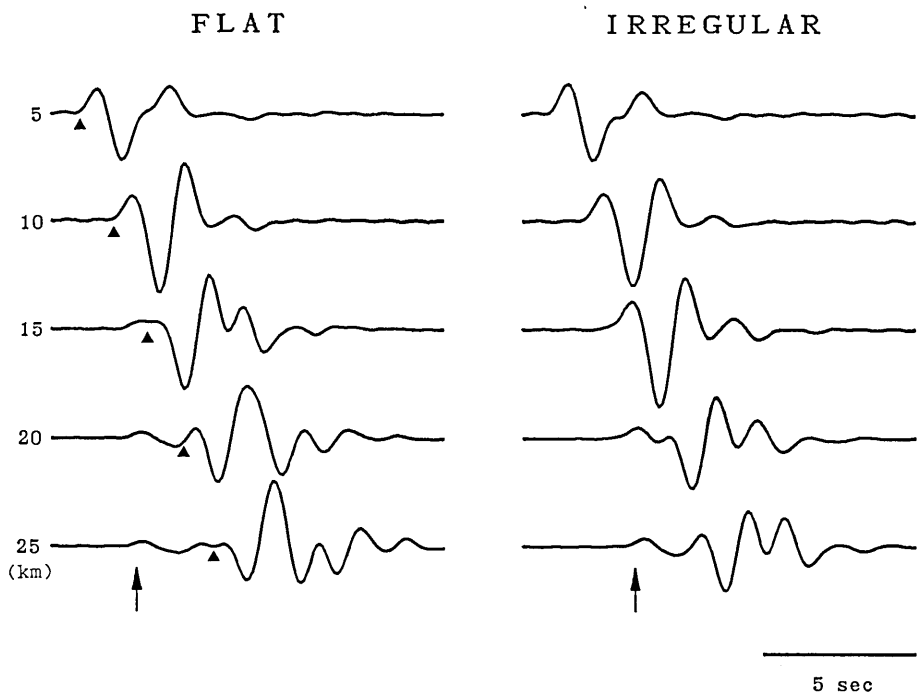

Fig. 2.14. Comparison of synthetic seismograms due to the line force computed for flat and two-dimensionally irregular structures. The irregular structure is shown in Fig. 2.13. The seismograms are reduced by the S velocity of the lower halfspace. Arrows and black triangles indicate the arrivals of head and direct waves, respectively.

50 km, $D=3$ km, and $C=2.5$ km. The line force is located 0.5 km deep in the center of the basin. We take $N=128$ and $\Delta k=2\pi/128$ km for the irregularity matrix.

The traces in the right half of Fig. 2.14 were computed for this structure. For the laterally homogeneous case the seismograms in Fig. 2.12 are presented in the left half to show the effect of the laterally heterogeneous structure. Both the irregular and flat interfaces generate clear head waves, which are indicated by arrows in the figure. Multiply reflected waves are coming a few seconds after the arrival of direct waves (▲ in the left half indicates the arrival of the direct waves). They are strongly distorted by the irregular interface.

(3) Point source

We are most interested in synthetic seismograms for a seismic point source, because an earthquake source is usually modeled as a point dislocation or a group of point dislocations. The wave-field of a

point source is generally expressed by a triple Fourier transform in the the Cartesian coordinates (x, y) and t. Since the triple inversion requires extensive computation, we use the Hankel transform in a cylindrical coordinate system (r, θ, z).

The displacement (u, v, w) in the cylindrical coordinates is written in potential form as

$$u=\frac{\partial \Phi}{\partial r}+\frac{\partial^2 \Psi}{\partial r \partial z}+\frac{1}{r}\frac{\partial X}{\partial \theta}$$
$$v=\frac{1}{r}\frac{\partial \Phi}{\partial \theta}+\frac{1}{r}\frac{\partial^2 \Psi}{\partial z \partial \theta}-\frac{\partial X}{\partial r}$$
$$w=\frac{\partial \Phi}{\partial z}+\frac{\partial^2 \Psi}{\partial z^2}-\nabla^2 \Psi \tag{54}$$

where

$$\Phi(r, \theta, z, t)=\frac{A(\theta)}{2\pi}\int_{-\infty}^{+\infty} e^{j\omega t}d\omega \int_0^{+\infty} \tilde{\Phi}(k, z, \omega)J_l(kr)dk$$
$$\Psi(r, \theta, z, t)=\frac{A(\theta)}{2\pi}\int_{-\infty}^{+\infty} e^{j\omega t}d\omega \int_0^{+\infty} \tilde{\Psi}(k, z, \omega)J_l(kr)dk$$
$$X(r, \theta, z, t)=\frac{\partial A(\theta)}{2\pi \partial \theta}\int_{-\infty}^{+\infty} e^{j\omega t}d\omega \int_0^{+\infty} \tilde{X}(k, z, \omega)J_l(kr)dk$$
$$A(\theta)=\text{radiation pattern},$$
$$J_l=\text{Bessel function } (l\text{-order}). \tag{55}$$

In u and v of the above equations we find the coupling of $P-SV$ and SH motions. However, if the near-field terms concerned with the coupling decay at long distances depending on $1/r$, their effects can be ignored except at very close distances, or at very low frequencies, as pointed out by WANG and HERRMANN (1980) and KOHKETSU (1985). When we neglect these near-field terms, (54) is reduced to the decoupled form

$$u=\frac{\partial \Phi}{\partial r}+\frac{\partial^2 \Psi}{\partial r \partial z}$$
$$v=-\frac{\partial X}{\partial r}$$
$$w=\frac{\partial \Phi}{\partial z}-\frac{\partial^2 \Psi}{\partial r^2}. \tag{56}$$

Under the similar approximation stress components are also reduced to

$$\tau_{rr}=(\lambda+2\mu)\frac{\partial u}{\partial r}+\lambda\frac{\partial w}{\partial z}, \qquad \tau_{\theta\theta}=\lambda\left(\frac{\partial u}{\partial r}+\frac{\partial w}{\partial z}\right),$$

$$\tau_{zz}=\lambda\frac{\partial u}{\partial r}+(\lambda+2\mu)\frac{\partial w}{\partial z}\ , \qquad \tau_{zr}=\mu\left(\frac{\partial u}{\partial z}+\frac{\partial w}{\partial r}\right)$$

$$\tau_{\theta z}=\mu\frac{\partial v}{\partial z}\ , \qquad \tau_{r\theta}=\mu\frac{\partial v}{\partial r}\ . \tag{57}$$

Comparing (55) and (57) with (3) and (4), we find that the basic equations in the cylindrical coordinates coincide with those in the Cartesian coordinates by the following substitutions:

$$x\to r\ ,\quad y\to\theta\ ,\quad e^{jkx}\to J_l(kr)\ ,$$

$$\varphi\to\Phi\ ,\quad \psi\to-\frac{\partial\Psi}{\partial r}\ ,\quad v\to-\frac{\partial X}{\partial r}\ . \tag{58}$$

Thus, when a $2-D$ medium depends on r and z, its elastic response to the point source can be computed in the far field with the same procedure as shown in the preceding sections. The discontinuity vector due to a point source can be calculated from the results of SATO (1972). The asymptotic expansion of the Bessel function

$$J_l(kr)\cong\frac{1}{\sqrt{2\pi kr}}\exp\left[-j\left(kr-\frac{(2l+1)\pi}{4}\right)\right] \tag{59}$$

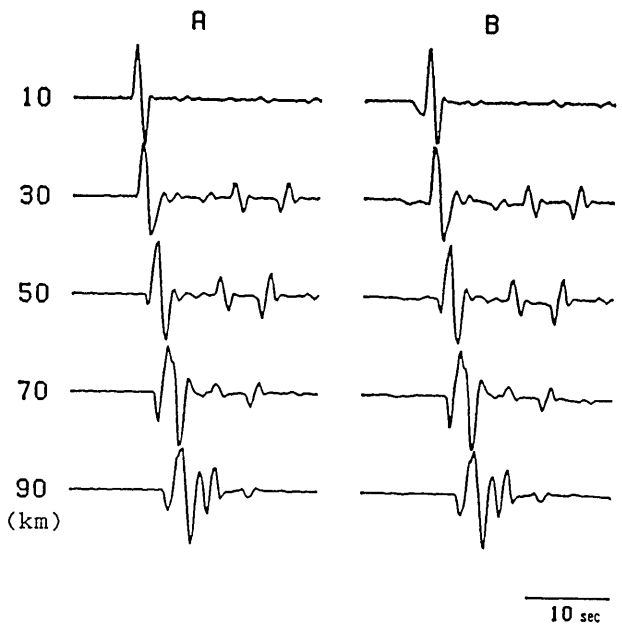

Fig. 2.15. Comparison of tangential displacements due to a point source computed without the near-field terms (**A**) or with them (**B**). The velocity model of Table 2.1 is used as a crustal structure.

Table 2.1. The Central U. S. model (after HERRMANN 1979)

d(km)	α(km/s)	β(km/s)	ρ(g/cm^3)
1	5.00	2.89	2.5
9	6.10	3.52	2.7
10	6.40	3.70	2.9
20	6.70	3.87	3.0
—	8.15	4.70	3.4

is also valid at distances where the near-field terms can be ignored.

Figure 2.15 illustrates a comparison between the seismograms in a $1-D$ medium computed with and without the near-field terms. They represent tangential displacements at 10, 30, 50, 70, and 90 km distances due to a vertical dip-slip source buried at a 10 km depth in the Central U.S. model (HERRMANN 1979, Table 2.1). HERRMANN'S (1979) source time function

$$f(t)=\begin{cases}0 & t\leqq 0\\ (t/\tau)^2/4\tau & 0<t\leqq\tau\\ (-(t/\tau)^2+4(t/\tau)-2)/4\tau & \tau<t\leqq 3\tau\\ ((t/\tau)^2-8(t/\tau)+16)/4\tau & 4\tau<t\leqq 4\tau\\ 0 & t>4\tau\end{cases} \tag{60}$$

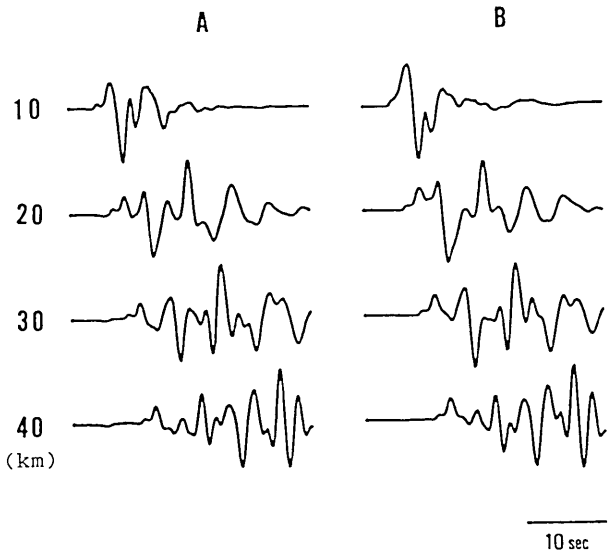

Fig. 2.16. Comparison of radial displacements due to a point source computed without the near-field terms (**A**) or with them (**B**). The velocity model of Table 2.2 is used as a crustal structure.

Table 2.2. The Tokyo model

d(km)	α(km/s)	β(km/s)	ρ(g/cm^3)
1.0	1.8	0.7	2.0
1.6	2.5	1.5	2.3
—	5.5	3.0	2.5

is used with $\tau=0.5$ sec. Although the seismograms in section (A) do not include the near-field terms, the two sections compare favorably. The difference appearing in the early part of the 10 km traces arises from the neglect of the terms in (A). Figure 2.16 compares radial displacements computed with and without the near-field terms. A strike-slip source with $\delta=80°$ and $\lambda=5°$ is buried at a six km depth in the crustal structure beneath Tokyo (Table 2.2). $Q_p=35$ and $Q_s=15$ are given to the top sedimentary layer. The source time function is the same as that for the previous example. The sections in Fig. 2.16 also compare favorably except for the top traces at the 10 km distance, which show the significant difference caused by the loss of SH waves in section (A). The asymptotic expansion (59) for the Bessel function may also lead to wrong waveforms. Thus these two examples show

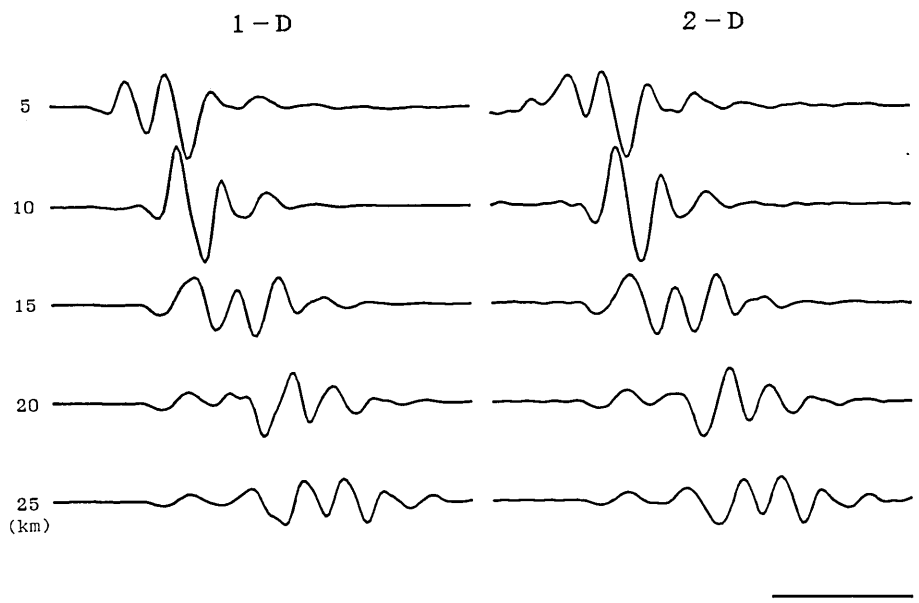

Fig. 2.17. Comparison of synthetic seismograms computed by the $1-D$ and $2-D$ reflectivity methods. The traces are tangential surface displacements at distances 5, 10, 15, 20 and 25 km from a point dislocation buried in the flat structure.

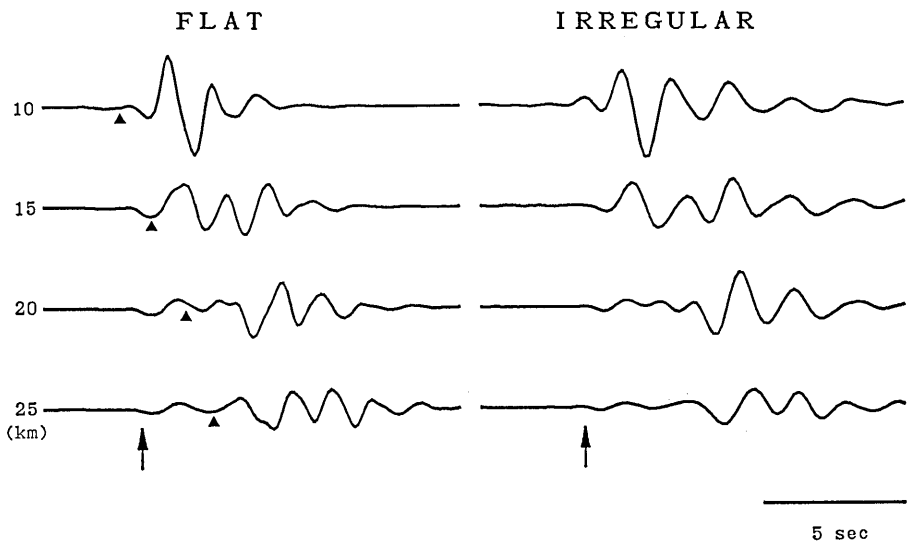

Fig. 2.18. Comparison of synthetic seismograms due to the point dislocation computed for the flat and two-dimensionally irregular structures. The irregular structure was shown in Fig. 2.13. The seismograms are reduced by the S velocity of the lower halfspace. Arrows and black triangles indicate the arrivals of head and direct waves, respectively.

that the near-field terms can be ignored and the asymptotic expansion (59) can be used at distances farther than 10 km from the source.

Figure 2.17 shows the synthetic seismograms which were computed by the $1-D$ and $2-D$ reflectivity methods for the flat structure in the previous section. A point source with vertical dip slip is buried at a depth of one km. The time function (60) is used with $\tau=0.5$ sec. Both the record sections agree with each other, except for the uppermost traces. Acausal arrivals arising from the neglect of the near-field terms contaminate the early part of the trace computed with the $2-D$ reflectivity method at $\Delta=5$ km.

The seismograms in the right half of Fig. 2.18 were calculated for the basin structure of Fig. 2.13. The interface is expressed by (48) with $D=3$ km and $C=1.0$ km, and the source is buried in the center of the basin. We take $N=128$ and $\Delta k=2\pi/320$ km for the irregularity matrix. Comparing them with the traces for the flat structure in the left half, we again find multiply reflected waves with distortion and clear head waves.

3. Effect of crustal models

In this chapter we will reveal how much the detail of a crustal

model affects synthetic seismograms using the method mentioned previously. Seismograms will be computed for typical models to investigate the effect of a thin layer, and that of an interface dent or trough. Our approach will also be applied to the actual structure beneath the Kanto plain.

3.1 Effect of crustal details

Here it is considered how synthetic seismograms are influenced by the details of crustal models. First we investigate the characteristics of *SH* waves travelling through a thin layer. A line force is buried at a depth of five km in a halfspace underlying a thin layer (Fig. 3.1). The velocity contrast between the upper layer and the lower halfspace is 2.0/3.6, which is rather low. Since $f(t)$ in (49) is used as the time function of the source force, the incident wave propagating into the layer has the time dependence represented by

$$\int_{-\infty}^{t} f(s)ds \ . \tag{61}$$

The layer may have various thicknesses. The seismograms in Fig. 3.2 are computed at 10 km, 30 km and 50 km for some particular layer thicknesses, *i.e.* $\lambda/60$, $\lambda/30$, $\lambda/10$, $\lambda/6$ and $\lambda/3$, where λ is the predominant wavelength of the incident wave in the halfspace. Comparing them to the top traces which are computed for the model without the layer, it is found that the layers of $\lambda/10$ or more strongly deform the seismograms. Especially, the traces at distances of 30 km and 50 km are contaminated by well-developed reverberation phases in

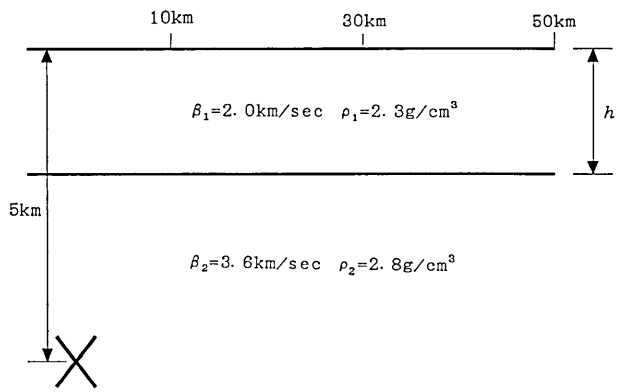

Fig. 3.1. Configuration of the crustal model studied. The upper layer may have various thicknesses (h). A big cross indicates the line force burried at a depth of 5 km.

Fig. 3.2. Comparison of the synthetic seismograms computed for various layer thicknesses. The values at the head of the leftmost seismograms indicate the layer thickness using the predominant wavelengh λ of incident waves.

the later portion. The traces for $\lambda/60$ and $\lambda/30$, on the other hand, have shapes quite similar to that of the top traces.

Secondly, we investigate how dents on interfaces affect *SH* waves propagating through them. A plane *SH* wave is impinging vertically from a halfspace into an overlying layer (Fig. 3.3). Its characteristics are represented by (49) and the predominant wavelength λ in the layer. On the interface there is a dent, whose width is 4λ. It may have various depths.

We consider two cases of the velocity contrast between the layer and the halfspace. Figure 3.4 shows the synthetic seismograms for the case of low velocity contrast ($\beta_1/\beta_2=1.7/3.5$). They are computed at the points *A*, *B* and *C* in Fig. 3.3. In the seismograms computed for dent depths of $\lambda/30$ and $\lambda/10$, the principal parts agree well with that of the top traces computed for a flat interface. In the seismograms of $\lambda/6$ and $\lambda/3$, however, reverberation phases contaminate

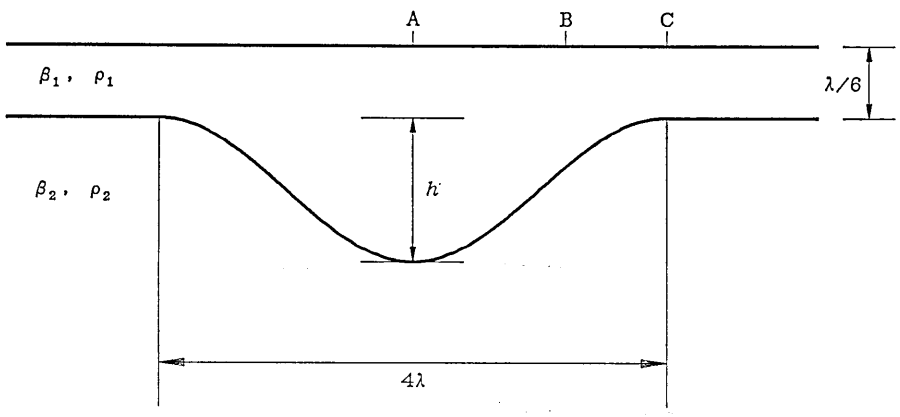

Low Contrast
β_1=1.7km/sec ρ_1=2.3g/cm^3
β_2=3.5km/sec ρ_1=3.3g/cm^3

High Contrast
β_1=0.7km/sec ρ_1=2.0g/cm^3
β_2=3.5km/sec ρ_1=3.3g/cm^3

Fig. 3.3. Configuration of the crustal model with a dent on the interface. A plane *SH* wave with the predominant wavelength λ is impinging vertically into the upper layer. The dent may have various depths (h). Two cases of velocity contrast are considered.

their principal parts.

The situation is more serious in the case of high velocity contrast (β_1/β_2=0.7/3.5, Fig. 3.5). The reverberation phases are strongly amplified even in the seismograms of $\lambda/30$. Moreover, they are very sensitive to the interface dent, and the seismograms in Fig. 3.5 have different shapes from each other.

The last example in this section is presented to show the effect of an interface trough on synthetic seismograms. The same line force as in Fig. 3.1 is buried in a layer three km thick overlying a halfspace (Fig. 3.6). The velocity contrast between the layer and the halfspace is rather low (β_1/β_2=2.0/3.6). A trough extends on the interface from 10 km to 30 km. It may have various depths.

The seismograms at the top of Fig. 3.7 are computed for the model without the trough. On these traces the arrivals of head and direct waves are indicated by △ and ▲, respectively. Comparing them to the seismograms for the trough depths of $\lambda/30$, $\lambda/10$ and $\lambda/6$, the arrival delay of head waves due to the trough is not obvious. However, the distortion by the trough can be seen, though the amplitudes of the head waves are very small.

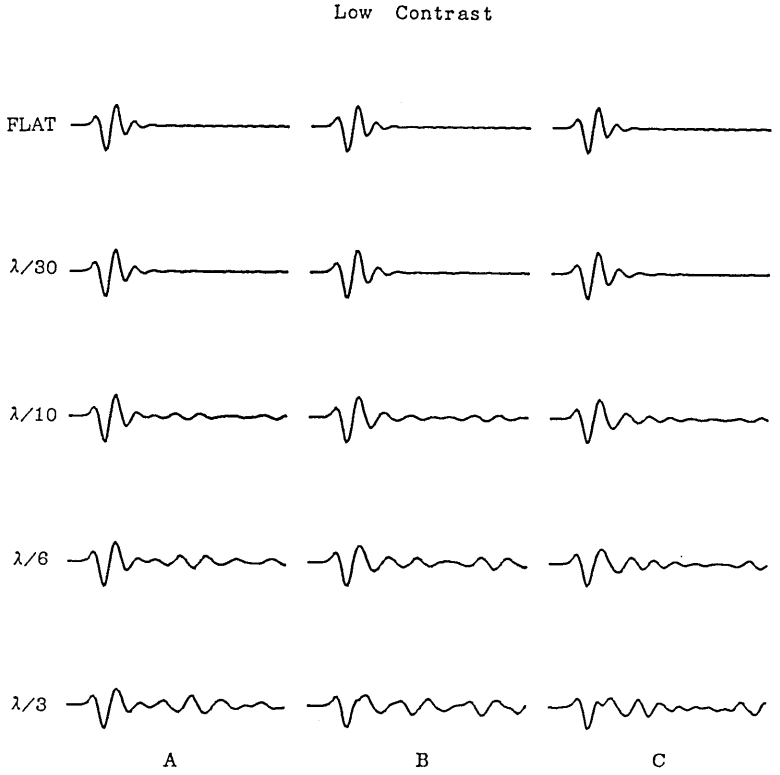

Fig. 3.4. Comparison of the synthetic seismograms at **A**, **B** and **C** (see Fig. 3.3) computed for various dent depths. The low velocity contrast is adopted. The values at the head of the leftmost seismograms indicate the dent depth using the predominant wavelengh λ of the incident wave.

Of course the direct waves are affected little by the trough. The trough delays the arrivals of reflected wave trains coming after the direct waves. This delay can be identified in the seismograms of $\lambda/10$ and $\lambda/6$ by the separation of the direct wave and the reflected wave train. Even in the leftmost seismograms observed in front of the trough, we find a small effect of the trough at the tail of the principal phase.

From the above three examples it can be said that layers thicker than a tenth of λ (λ: wavelength of an incident wave), and interface dents or troughs larger than a tenth of λ may affect synthetic seismograms. Reverberations in low velocity sediments may suffer very strong effects by them. Thus, seismograms which are computed ignoring them may lead to wrong estimations of medium effects.

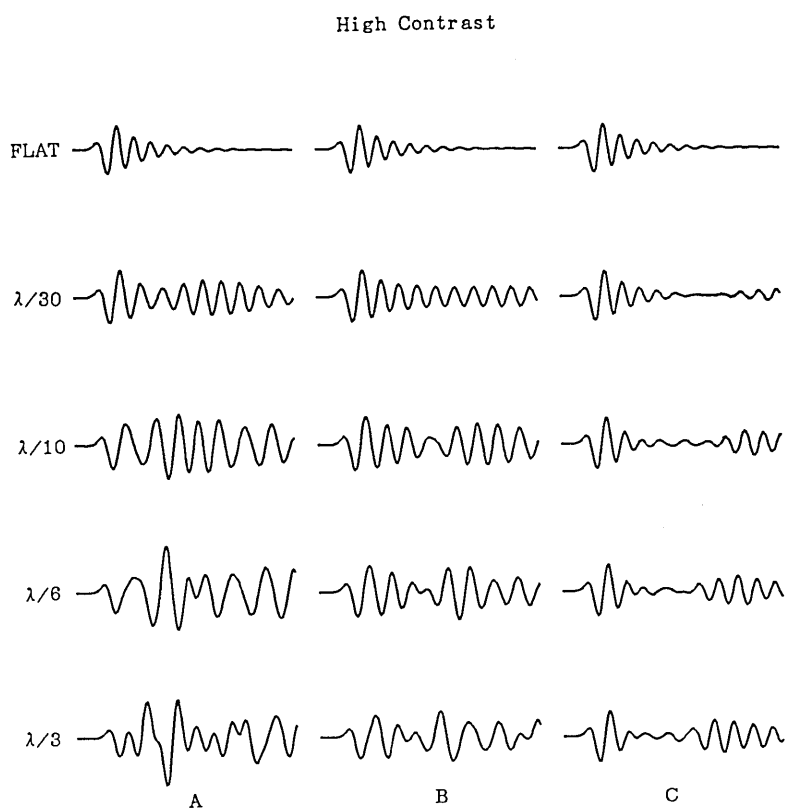

Fig. 3.5. Comparison of the synthetic seismograms at **A, B** and **C** (see Fig. 3.3) computed for various dent depths. The high velocity contrast is adopted. The values at the head of the leftmost seismograms indicate the dent depth using the predominant wavelengh λ of the incident wave.

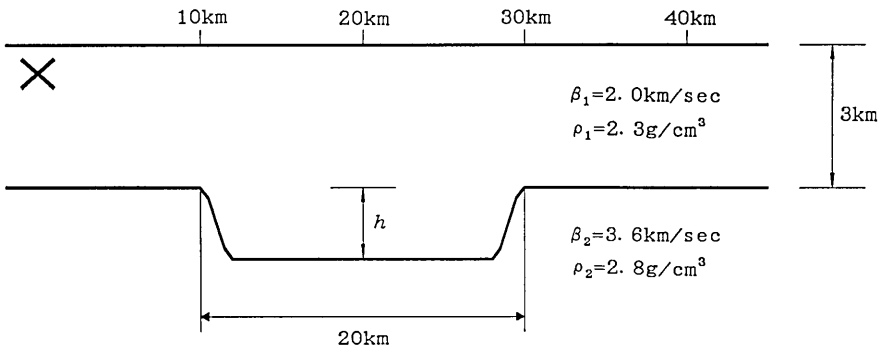

Fig. 3.6. Configuration of the crustal model with a trough on the interface. The trough may have various depths (h). The big cross indicates the line force buried at a depth of 0.5 km.

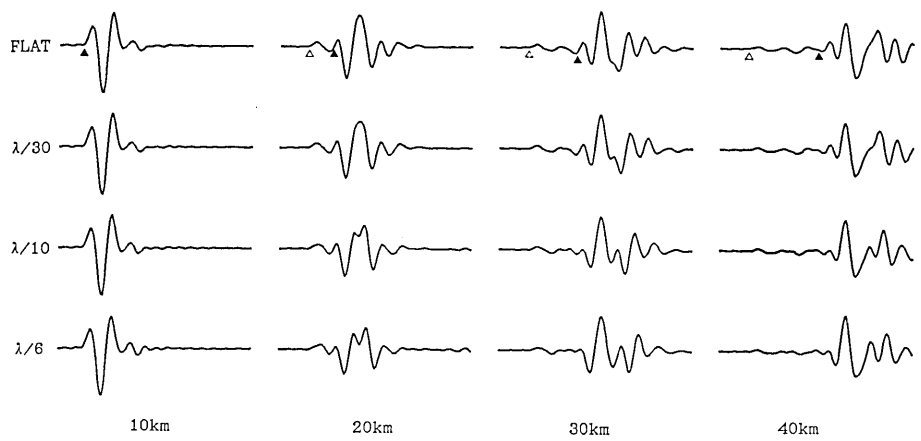

Fig. 3.7. Comparison of the synthetic seismograms computed for various trough depths. On the traces computed for the flat interface, △ and ▲ indicate the arrivals of the head and direct waves, respectively. The values at the head of the leftmost seismograms indicate the trough depth using the predominant wavelengh λ of incident waves.

3.2 Seismograms in the Kanto plain

(1) Two-dimensional structure

Finally we apply our approach to compute synthetic seismograms in the Kanto plain. The shallow structure in and beneath the Kanto plain has been investigated in detail by more than 20 refraction experiments (SHIMA *et al.* 1976a, b, 1978a, b, 1981) and *in situ* measurements at deep boreholes (TAKAHASHI and HAMADA 1975, OHTA *et al.* 1981).

The three layers of Table 3.1 have already been revealed. The influence of Q cannot be ignored, because even in the near-field seismograms may be distorted by such a low Q as expected for sediments (TAKEO 1985). The Q_p values on Table 3.1 were estimated by KOHKETSU and SHIMA (1985) from a comparison of observed and synthetic explosion seismograms.

The 6-th, 12-th and 21-th Yumenoshima experiments were carried out along the Yumenoshima-Hatoyama profile, which extends from

Table 3.1. Velocity model in the Kanto Plain

α(km/s)	β(km/s)	ρ(g/cm^3)	Q_p
1.8	0.68	2.0	35
2.7	1.5	2.3	100
5.5	3.0	2.5	400

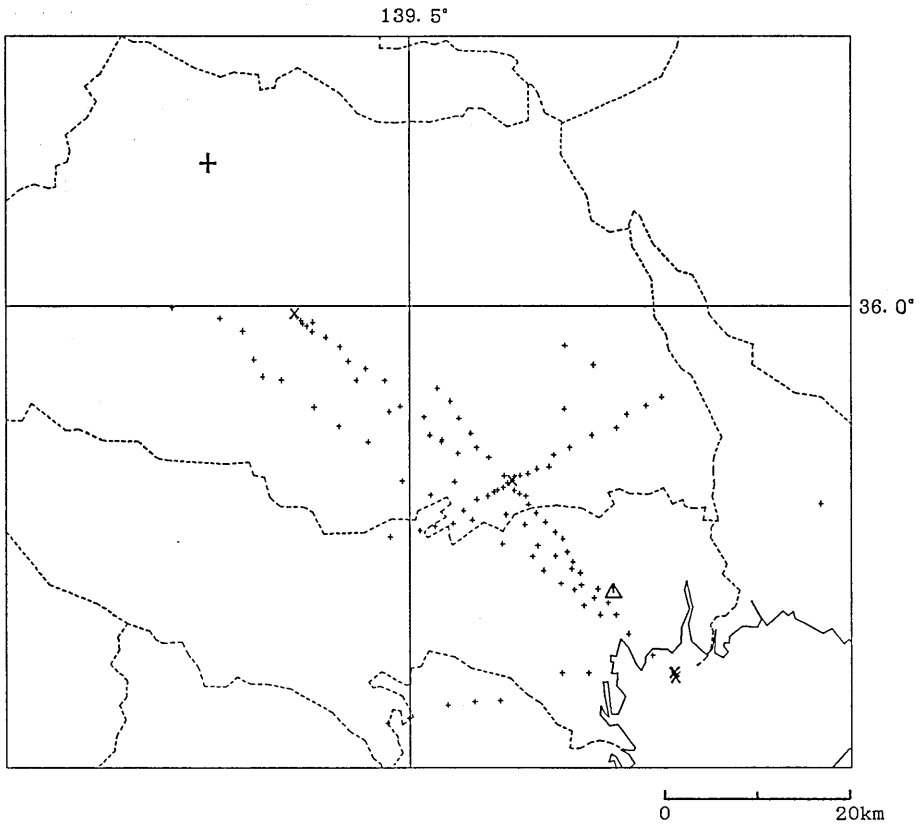

Fig. 3.8. Map around Tokyo. The shot and observation points of refraction experiments are indicated by big cross and small plus signs. A big plus sign and a triangle indicate the epicenter of the Saitama earthquake of 1931 and the Earthquake Research Institute, respectively.

Tokyo in the *NW* direction. They were followed by the reverse experiments of the Hotoyama and Bijoki explosions. Figure 3.8 shows the shot points (big cross) and the observation points (small plus signs) of these experiments.

The $2-D$ structure along this profile is obtained by comparing the observed and calculated travel times. The travel time calculation for $2-D$ media is performed by the ray tracing program *SEIS*83 (Červený and Pšenčík 1983). The result of the 6-th Yumenoshima experiment is shown in Fig. 3.9. In the right diagram big crosses and small plus signs indicate observed and calculated travel times, respectively. The interface separating the sediments and the basement has a basin shape except for the velocity anomaly around 45 km. The phase appearing beyond 55 km with a high velocity is considered to

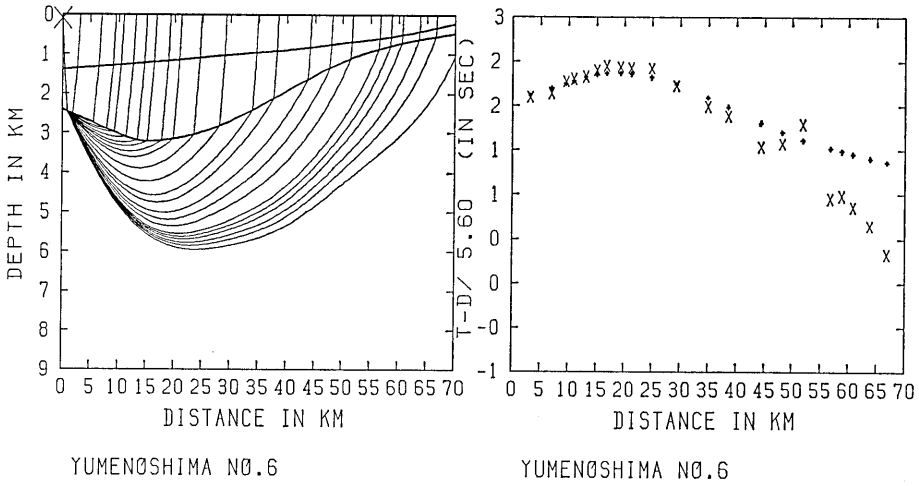

Fig. 3.9. Ray and travel time diagrams for the 6-th Yumenoshima refraction experiment.

come from a deeper part of the medium.

The shape of the first interface is not determined well, because the phase traveling along it could not be detected except at the vicinity of the explosive sources.

(2) Seismograms for a point source

We here show the effect of the two-dimensionally layered attenuative sediments in the Kanto plain on long-period synthetic seismograms. The Saitama earthquake occurred in 1931 at the north-western part of the Kanto plain, and seismograms were obtained at the Earthquake Research Institute, the University of Tokyo. As shown in Fig. 3.8 the epicenter and the ERI are located on the Yumenoshima-Hatoyama profile. Then we compute synthetic seismograms of this earthquake for a variety of crustal models. Since we cannot compute seismograms for a finite fault in a $2-D$ medium by the current computer facility, only SH waves due to a point dislocation are computed. From the results of ABE (1974) the source is assumed to be with a vertical

Table 3.2. Crustal models

	d(km)	β(km/s)	ρ(g/cm^3)	Q_s
Model F, H		3.5	2.8	∞
Model M	1.5	1.2	2.2	∞
	—	3.2	2.5	∞
Model MQ	1.5	1.2	2.2	40
MQ2	—	3.0	2.5	200

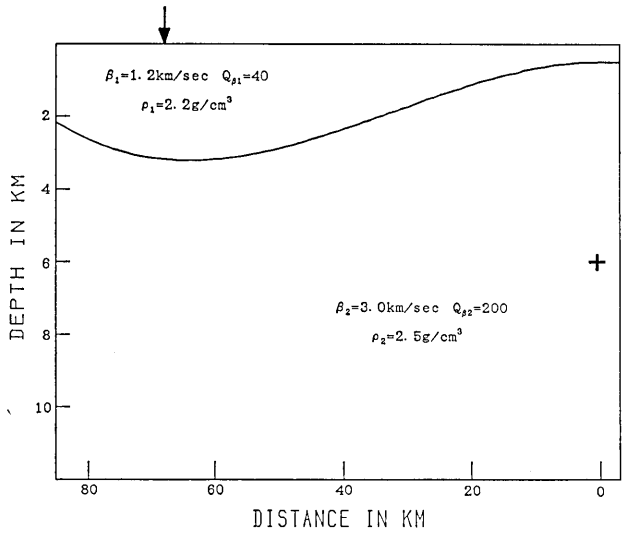

Fig. 3.10. Simplified two-dimensional structure along the Yumenoshima-Hatoyama profile. A big plus sign and an arrow indicate the point source and the observation point, respectively.

strike slip at a depth of six km.

We consider four models in Table 3.2. Model F is an infinite space, and Model H is a halfspace with the same material parameters as Model F. Model M is the simplified $1-D$ structure along the Yumenoshima-Hatoyama profile. Since the first interface cannot be determined well, the two sedimentary layers are combined into a 1.5 km thick layer with $\beta=1.2$ km/sec and $\rho=2.2$ g/cm^3. Attenuation is considered in Model MQ. The Q_s values are estimated from the Q_p values on Table 3.1 with the relation $Q_s/Q_p=4/9$. Finally the irregularity of the interface between the sediment and the basement is considered in Model MQ2. The interface shape is presented in Fig. 3.10. The source and the ERI are also indicated by a big plus sign and an arrow in the figure.

We computed seismograms for a long-period seismograph installed at the ERI ($\Delta=68$ km) with adjustments for arrival times. The seismograms for Model F are computed by the method of SATO (1975) and doubled for including the effect of the free surface. Figure 3.11 shows the computed seismograms for the crustal models. It is clearly found that a waveform is distorted more and an overall amplitude becomes greater, when the crustal model comes close to the actual structure (from Model F to Model MQ2). Especially, the trace for Model MQ2 is strongly amplified and distorted by a thick sediment beneath the

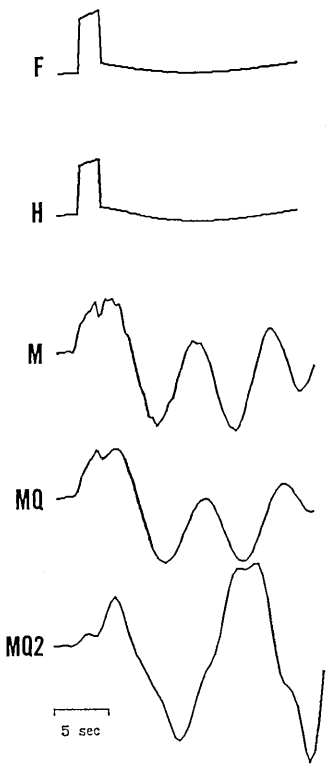

Fig. 3.11. Synthetic seismograms due to the fixed point source for the variety of crustal structures listed in Table 3.2.

observation point. Comparing the traces for Models M and MQ, we also find that the low Q value of the sediment reduces the amplitude of the later potion of the trace MQ. During the initial half cycle they have a similar waveform.

These distortions and amplifications, or the reduction by the attenuative sediment must appear in synthetic seismograms for a finite fault source. The reason for this is that they are synthesized by summing up seismograms for point sources distributed over the fault.

4. Conclusion

The reflectivity method is extended to compute synthetic SH and $P-SV$ seismograms in one- and two-dimensionally layered media. We introduce the Fourier transform technique of AKI and LARNER (1970) to solve the integral equations for the two-dimensional boundary conditions and enlarge the propagator matrices to express the total wave-field. Numerical examples are also presented for structures consisting of homogeneous layers separated by irregular interfaces.

Our method can be applied to vertically inhomogeneous layers by using appropriate propagator-matrix elements (*e.g.*, WOODHOUSE 1978; KENNETT and ILLINGWORTH 1981). Because of limitations of the Fourier transform, seismograms cannot be computed for a block structure or a vertical discontinuity.

At present two computational problems still remain. First, we have no analytical expression for the inverse of irregularity matrix, $\mathbf{K}^{-1}$. When the interfaces are highly irregular, off-diagonal elements of the submatrices of $\mathbf{K}$ grow so large that a numerical inversion

breaks down, or large noises remain. These noises may become much larger if seismic waves propagate through many irregular interfaces.

Secondly, our method also suffers the overflow errors related to high frequencies, slow phase velocities and thick layers as in the $1-D$ reflectivity method. It is not so serious in *SH*-waves calculations, but for $P-SV$ waves we havo to introduce some techniques such as delta matrix extension (DUNKIN 1965) and normalization (HARVEY 1981), or to reformulate the problem without the propagator matrices (KENNETT 1980; HA 1984). Recently KENNETT (1986) extended his formulation to three-dimensionally heterogeneous media by extracting terms associated with heterogeneity.

If we neglect the coupling between the *SH* and $P-SV$ wave-fields, the extension to a three-dimensional structure is straightforward. However, we should carry out a double Fourier transform with respect to both x and y coordinates to construct the irregularity matrix $\mathbf{K}$, and the linear equation system for the condition of continuity is expanded into $8N\times 8N$ or $4N\times 4N$ equations. Since it takes 10 (plane wave incidences) or 30 (point sources) minutes for Hitachi M-280H (15 MIPS) to compute the numerical examples in this paper, a three-dimensional computation requires 100 or 900 minutes.

To illustrate the effects of the details of crustal models on synthetic seismograms, several examples are presented. Numerical simulations reveal that surface layers thicker than $\lambda/10$ (λ: wavelength of an incident wave) cannot be ignored, and interface dents or troughs larger than $\lambda/10$ can affect seismograms.

The results of refraction experiments (*e.g.*, SASAKI *et al.* 1970, AOKI *et al.* 1972) and travel-time analyses of natural earthquakes (*e.g.*, UKAWA and FUKAO 1981) show that the main body of the crust ($V_p=6\sim7$ km/sec, $V_s=3\sim4$ km/sec) does not reach the Earth's surface. There are several layers separating them, and their interfaces often have irregular shape. When we analyze seismic waves in the crust with a dominant frequency of 1/5 Hz, layers thicker than one km and interface dents larger than one km should be taken into account.

If those are neglected, synthetic seismograms lead to wrong estimations of medium effects. For example, the source models of Japanese earthquakes were mostly derived with synthetic seismograms for infinite or semi-infinite crustal models. They certainly include some errors.

Acknowledgements

I would like to express sincere thanks to Profs. Etsuzo Shima,

Ryosuke Sato and Shuzo Asano for many suggestions and encouragements throughout this study. Profs. Yukio Hagiwara, Toshikatsu Yoshii and Katsuyuki Abe, and Drs. Kiyoshi Takano and Takashi Miyatake allowed me to study freely.

Discussions with Profs. Robert Geller, Brian Kennett, Vlastislav Červený, and Drs. Naoshi Hirata, Kiyoshi Yomogida, Rainer Kind and C. Y. Wang are very helpful. Members of the seminars sponsored by Profs. Ryosuke Sato and Takuo Maruyama gave me helpful comments. Prof. Keiiti Aki, Drs. David Boore and Robert Nowack, the American Geophysical Union, and the Seismological Society of America kindly permitted me to reproduce their copyrighted figures. Mr. Iwashita gave me a result of the finite element computation. I am also grateful to Drs. R. Kind, Ichiro Kawasaki and Hiroshi Kanazawa for their computer programs. Anonymous reviewers pointed out careless mistakes to me.

This study is the main part of the *Ph.D.* thesis accepted by the Faculty of Science, the University of Tokyo. It was supported by Grants-in-Aid for Scientific Research (No. 57025011, 59025009 and 61025012) from the Ministry of Education, Science and Culture of Japan. The computations were carried out at the Earthquake Prediction Data Center, the Earthquake Research Institute, and at the Computer Centre, the University of Tokyo.

References

ABE, K., 1974, Seismic displacement and ground motion near a fault: The Saitama earthquake of September 21, 1931, *J. Geophys. Res.* **79**, 4393-4399.

AKI, K. and P. G. RICHARDS, 1980, *Quantitative Seismology: Theory and Methods*, W. H. Freeman and Company, San Francisco, California.

AKI, K. and K. L. LARNER, 1970, Surface motion of a layered medium having an irregular interface due to incident plane *SH* waves, *J. Geophys. Res.* **75**, 933-954.

ALEKSEEV, A. S. and B. G. MIKHAILENKO, 1980, The solution of dynamic problems of elastic wave propagation in inhomogeneous media by a combination of partial separation of variables and finite-difference methods. *J. Geophys.*, **48**, 161-172.

AOKI, H., T. TADA, Y. SASAKI, T. OOIDA, I. MURAMATU, H. SHIMAMURA and I. FURUYA, 1972, Crustal structure in the profile across Central Japan as derived from explosion seismic observations, *J. Phys. Earth*, **20**, 197-223.

APSEL, R. J. and J. E. LUCO, 1983, On the Green's functions for a layered half-space, Part II, *Bull. Seism. Soc. Am.*, **73**, 931-951.

BARD, P. Y. and M. BOUCHON, 1980, The seismic response of sediment-filled valleys. Part 1. The case of incident *SH* waves, *Bull. Seism. Soc. Am.*, **70**, 1263-1286.

BOORE, D. M., 1970, Love waves in nonuniform wave guides: Finite difference calculations, *J. Geophys. Res.*, **75**, 1512-1527.

BOORE, D. M., 1972, A note on the effect of simple topography on seismic *SH* waves, *Bull. Seism. Soc. Am.*, **62**, 275-284.

BOORE, D. M., K. L. LARNER and K. AKI, 1971, Comparison of two independent methods

for the solution of wave-scattering problems: Response of a sedimentary basin to vertically incident *SH* waves, *J. Geophys. Res.* **76**, 558-569.

BOUCHON, M., 1979, Discrete wave number representation of elastic wave fields in three-space dimensions, *J. Geophys. Res.*, **84**, 3609-3614.

BOUCHON, M., 1981, A simple method to calculate Green's functions for elastic layered media, *Bull. Seism. Soc. Am.*, **71**, 959-971.

ČERVENÝ, V., 1983, Synthetic body wave seismograms for laterally varying layered structures by the Guassian beam method, *Geophys. J. R. Astr. Soc.*, **73**, 389-426.

ČERVENÝ, V., I. A. MOLOTKOV, and I. PŠENČIK, 1977, *Ray Method in Seismology*, Karlova Universita, Praha.

ČERVENÝ, V. and I. PŠENČÍK, 1983, *Program SEIS*83, Karlova Universita, Praha.

ČERVENÝ, V. and R. RAVINDRA, 1971, *Theory of seismic head waves*, Univ. Toronto Press, Toronto.

CHAPMAN, C. H., 1978, A new method for computing synthetic seismograms, *Geophys. J. R. Astr. Soc.*, **54**, 481-518.

CORMIER, V. F., 1980, The synthesis of complete seismograms in an earth model specified by radially inhomogeneous layers, *Bull. Seism. Soc. Am.*, **70**, 691-716.

CORMIER, V. F. and P. G. RICHARDS, 1977, Full wave theory applied to a discontinuous velocity increase: the inner core boundary, *J. Geophys.*, **43**, 3-31.

CUNDALL, P. A., R. R. KUNAR, P. C. CARPENTER and J. MARTI, 1978, Solution of infinite dynamic problems by finite modelling in the time domain, *Proc. 2nd Int. Conf. Appl. Num. Modelling*, Madrid, Spain.

DUNKIN, J. W., 1965, Computation of modal solutions in layered media at high frequencies, *Bull. Seism. Soc. Am.*, **55**, 335-358.

FABER, S. and G. MÜLLER, 1980, S_p phases from the transition zone between the upper and lower mantle, *Bull. Seism. Soc. Am.*, **58**, 179-214.

FUCHS, K., 1968. The reflection of spherical waves from transition zones with arbitrary depth-dependent elastic moduli and density, *J. Phys. Earth.* **16**, Special Issue, 27-41.

FUCHS, K. and G. MÜLLER, 1971, Computation of synthetic seismograms with the reflectivity method and comparison with observations, *Geophys. J. R. Astr. Soc.*, **23**, 417-433.

HA, J., 1984, Recurrence relations for computing complete *P* and *SV* seismograms, *Geophys. J. R. Astr. Soc.*, **79**, 863-873.

HARKRIDER, D. G., 1964, Surface waves in multilayered elastic media. 1. Rayleigh and Love waves from buried sources in a multilayered half-space, *Bull. Seism. Soc. Am.*, **54**, 627-679.

HARVEY, D. J., 1981, Seismograms synthesis using normal mode superposition: The locked mode approximation, *Geophys. J. R. Astr. Soc.*, **66**, 37-69.

HASKELL, N. A., 1953, The dispersion of surface waves on multilayered media, *Bull. Seism. Soc. Am.*, **43**, 17-34.

HELMBERGER, D. V., 1968, The crust-mantle transition in the Bering Sea, *Bull. Seism. Soc. Am.*, **58**, 179-214.

HERRMANN, R. B., 1979, *SH*-wave generation by dislocation sources -A numerical study, *Bull. Seism. Soc. Am.*, **69**, 1-15.

HONG, T. L. and D. V. HELMBERGER, 1978, Glorified optics and wave propagation in non-planar structure, *Bull. Seism. Soc. Am.*, **68**, 1313-1330.

HONG, T. L. and D. KOSLOFF, 1978, An application of the finite element method in wave propagation problems involving irregular structures (in preparation).

HRON, F. and E. R. KANASEWICH, 1971, Synthetic seismograms for deep seismic sounding studies using asymptotic ray theory, *Bull. Seism. Soc. Am.*, **61**, 1169-1200.

KENNETT, B. L., 1980, Seismic waves in a stratified half space. II. Theoretical seismograms, *Geophys. J. R. Astr. Soc.*, **61**, 1-10.

KENNETT, B. L., 1986, Wavenumber and wavetype coupling in laterally heterogeneous media, *Geophys. J. R. Astr. Soc.*, **87**, 313-331.

KENNETT, B. L. and M. R. ILLINGWORTH, 1981, Seismic waves in a stratified half space. III. Piecewise smooth models, *Geophys. J. R. Astr. Soc.*, **66**, 633-675.

KENNETT, B. L. and N. J. KERRY, 1979, Seismic waves in a stratified half space, *Geopys. J. R. Astr. Soc.*, **57**, 557-584.

KIND, R., 1978, The reflectivity method for a buried source, *J. Geophys.*, **44**, 603-612.

KOHKETSU, K., 1981, Reinterpretation of seismograms obtained by the Kurayosi explosions with the reflectivity method, *J. Phys. Earth*, **29**, 255-265.

KOHKETSU, K., 1985, The extended reflectivity method for synthetic near-field seismograms, *J. Phys. Earth*, **33**, 121-131.

KOHKETSU, K., 1987, 2—D reflectivity method and synthetic seismograms in irregularly layered structures. I. *SH*-wave generation, *Geophys. J. R. Astr. Soc.*, **89**, 821-838.

KOHKETSU, K. and E. SHIMA, 1985, Q_p structure of sediments in the Kanto plain, *Bull. Earthq. Res. Inst., Univ. Tokyo*, **60**, 495-505.

MÜLLER, G., 1969, Theoretical seismograms for some types of point sources in layered media. Part III: Single force and dipole sources of arbitrary orientation, *Z. Geophys.*, **35**, 347-371.

NOWACK, R. and K. AKI, 1984, The two-dimensional Gaussian beam synthetic method: Testing and application, *J. Geophys. Res.*, **89**, 7797-7819.

OHTA, Y., N. GOTO, F. YAMAMIZU and H. TAKAHASHI, 1980, *S*-wave velocity measurements in deep soil deposit and bedrock by means of an elaborated down-hole method, *Bull. Seism. Soc. Am.*, **70**, 363-377.

OLSON, A. H., J. A. ORCUTT, and G. A. FRAZIER, 1984, The discrete wavenumber/finite element method for synthetic seismograms, *Geophys. J. R. Astr. Soc.*, **77**, 421-460.

SASAKI, Y., S. ASANO, I. MURAMATSU, M. HASHIZUME, and T. ASADA, 1970, Crustal structure in the western part of Japan derived from the observation of the first and second Kurayosi and the Hanabusa explosions (continued), *Bull. Earthq. Res. Inst., Univ. Tokyo*, **48**, 1129-1136, 1970.

SATO, R., 1972, Seismic waves in the near field, *J. Phys. Earth*, **20**, 357-375.

SATO, R., 1975, Fast computation of theoretical seismograms for an infinite medium. Part I. Rectangular fault, *J. Phys. Earth*, **23**, 323-331.

SATO, R. and N. HIRATA, 1980, One method to compute theoretical seismograms in a layered medium, *J. Phys. Earth*, **28**, 145-168.

SHIMA, E., M. YANAGISAWA, K. KUDO, T. YOSHII, Y. ICHINOSE, K. SEO, K. YAMAZAKI, Y. OHBO, Y. YAMAMOTO, Y. OGUCHI and M. NAGANO, 1976a, On the base rock of Tokyo, *Bull. Earthq. Res. Inst., Univ. Tokyo*, **51**, 1-11 (in Japanese).

SHIMA, E., M. YANAGISAWA, K. KUDO, K. SEO and K. YAMAZAKI, 1976b, On the base rock of Tokyo II, *Bull. Earthq. Res. Inst., Univ. Tokyo*, **51**, 45-61 (in Japanese).

SHIMA, E., M. YANAGISAWA, K. KUDO, T. YOSHII, K. SEO, and K. KUROHA, 1978a, On the base rock of Tokyo III, *Bull. Earthq. Res. Inst., Univ. Tokyo*, **53**, 305-318 (in Japanese).

SHIMA, E., M. YANAGISAWA, K. KUDO, T. YOSHII, K. SEO, N. OHBO, T. HOSHINO, and M. NAGANO, 1978b, On the base rock of Tokyo IV, *Bull. Earthq. Res. Inst., Univ. Tokyo*, **53**, 1245-1255 (in Japanese).

SHIMA, E. M. YANAGISAWA, and K. KUDO, 1981, On the base rock of Tokyo V, *Bull. Earthq. Res. Inst., Univ. Tokyo*, **56**, 265-276 (in Japanese).

SMITH, W. D., 1975, The application for finite element analysis to body wave propagation problems, *Geophys. J. R. Astr. Soc.*, **42**, 747-768.

SPUDICH, P. and U. ASCHER, 1983, Calculation of complete theoretical seismograms in vertically varying media using collocation method, *Geophys. J. R. Astr. Soc.*, **75**, 101-124.

TAKAHASHI, H. and K. HAMADA, 1975, Deep-borehole observation of the Earth's crust

activities around Tokyo -Introduction of the Iwatsuki observatory, *Pure Appl. Geophys.*, **113**, 311-320.

TAKEO, M., 1985, Near-field synthetic seismograms taking into account the effects of anelasticity, *Papers Meteorol. Geophys.*, **36** (in Japanese).

UKAWA, M. and Y. FUKAO, 1981, Poisson's ratios of the upper and lower crust and the sub-Moho mantle beneath central Honshu, Japan, *Tectonophysics*, **77**, 233-256.

WANG, C. Y. and R. B. HERRMANN, 1980, A numerical study of *P*-, *SV*- and *SH*- wave generation in a plane layered medium, *Bull. Seism. Soc. Am.*, **70**, 1015-1036.

WOODHOUSE, J. H., 1978, Asymptotic results for elastodynamic propagator matrices in plane stratified and spherically stratified earth models, *Geophys. J. R. Astr. Soc.*, **54**, 263-280.

現実的媒質における理論地震記象：波動論的アプローチ

地震研究所　纐纈一起

地震記録を解析するためには，地震波を発生させた震源の影響と地震波を伝播させる媒質の影響を，記録から正しく分離しなければならない．媒質の影響は通常，理論地震記象を計算して評価される．従来この評価に際して，簡単な場合には無限媒質や半無限媒質，特に考慮される場合でも水平成層構造に対して地震記象を計算することで済まされてきた．ところが人工地震探査などの結果は，地球内部にいくつもの不規則な境界面があることを示しており，従来のやり方では正しく媒質の影響を評価できない．本研究ではより現実的な媒質モデルとして不規則成層構造を考え，波動論のアプローチで，それにおける完全な理論地震記象の計算方法を提案する．

まず変位と応力は二重フーリエ変換し，周波数・波数領域で運動応力ベクトルとしてとり扱う．水平成層構造ならば，境界面における境界条件は波数ごとに定義される運動応力ベクトルと伝播子行列で満たされるので，独立に計算された変位スペクトルを集めて逆変換すれば地震記象は求まる．ところが不規則な境界面では，散乱により異なった波数の変位スペクトルの間でカップリングが起って，境界条件を波数ごと独立にとり扱うことはできなくなり，積分方程式の形で残ってしまう．そこでここではこの積分方程式を解く方法として安芸・Larner によるフーリエ変換の方法を導入し，運動応力ベクトルや伝播子行列も，考慮すべきすべての波数要素を含むような形に拡張する．これらにより波動場を構成する変位スペクトル全体が一挙に求まり，それらを逆変換すれば不規則成層構造の理論地震記象を計算できる．

以上の方法の妥当性を見るため，いくつかの構造に対して地震記象を計算し，他の方法による計算結果との比較を行った．人工反射波の問題がない時，有限要素法は正しい記象を与えられると考えられるが，本研究による記象はこれによく一致している．しかも本研究の方法は有限要素法より高速で，事前に媒質を要素に分解する必要もない．近似法である波線理論や Gaussian Beam 法は，記象の後半部で破綻しており，正しい波形を与えていない．

このほか本研究の方法でシミュレーションを行い，どのくらいの厚さの表層が地震記象に影響するか，あるいは境界面にあるどの程度の大きさの凹部が地震記象に影響するかを調べた．結果はともに，入射波の波長の 10 分の 1 程度のものから効いてくることが示された．また実際的な応用として，関東平野の堆積層の 2 次元構造を求め，地殻最上部に置かれた点震源の地震記象を計算した．求めた構造の影響を見るため，計算結果を，地殻を無限媒質や半無限媒質とした場合，あるいは水平成層構造で Q 値を考慮しない場合と，した場合の記象と比較した．堆積層の存在，あるいは不規則境界面の影響は計算結果に強く現われており，さらに Q 値の影響は記象の後半に振幅を抑える形で現われることが示された．